J. Fluid Mech. (2007), *vol.* 581, *pp.* 97–127. © 2007 Cambridge University Press
doi:10.1017/S002211200700554X Printed in the United Kingdom

Diffuse-interface modelling of droplet impact

V. V. KHATAVKAR[1], P. D. ANDERSON[1],
P. C. DUINEVELD[2]† AND H. E. H. MEIJER[1]

[1]Materials Technology, Dutch Polymer Institute, Eindhoven University of Technology,
PO box 513, 5600 MB Eindhoven, The Netherlands
p.d.anderson@tue.nl

[2]Philips Research, Prof. Holstlaan, 4, 5656 AA, Eindhoven, The Netherlands

(Received 2 November 2005 and in revised form 5 December 2006)

The impact of micron-size drops on a smooth, flat, chemically homogeneous solid surface is studied using a diffuse-interface model (DIM). The model is based on the Cahn–Hilliard theory that couples thermodynamics with hydrodynamics, and is extended to include non-90° contact angles. The (axisymmetric) equations are numerically solved using a combination of finite- and spectral-element methods. The influence of various process and material parameters such as impact velocity, droplet diameter, viscosity, surface tension and wettability on the impact behaviour of drops is investigated. Relevant dimensionless parameters are defined and, depending on the values of the Reynolds number, the Weber number and the contact angle, which for the cases considered here range from 1.3 to 130, 0.43 to 150 and 45° to 135°, respectively, the model predicts the spreading of a droplet with or without recoil or even rebound of the droplet, totally or partially, from the solid surface. The wettability significantly affects the impact behaviour and this is particularly demonstrated with an impact at $Re = 130$ and $We = 1.5$, where for $\theta < 60^\circ$ the droplet oscillates a few times before attaining equilibrium while for $\theta \geqslant 60^\circ$ partial rebound of the droplet occurs, i.e. the droplet breaks into two unequal sized drops. The size of the part that remains in contact with the solid surface progressively decreases with increasing θ until at a value $\theta \approx 120^\circ$ a transition to total rebound happens. When the droplet rebounds totally, it has a top-heavy shape.

1. Introduction

Impact of drops on solid surfaces is central in many existing and emerging technologies such as inkjet printing, spray coating, DNA microarrays, solder-jet technology, spray cooling, application of pesticides etc. Such a diversity of applications usually implies that the physical and operating conditions cover a broad range and may include fluid dynamics, heat transfer and phase changes. Numerous studies of the process employing theoretical, experimental and numerical techniques have been reported since the original work done by Worthington (1876). A brief account of previous work in the field is provided here; for an exhaustive survey see the review by Rein (1993) whereas recent studies are summarized in Gunjal, Ranade & Chaudhari (2005). Theoretical analyses, e.g. by Chandra & Avedisian (1991), Pasandideh-Fard *et al.* (1996), Mao, Kuhn & Tran (1997) and Roisman, Rioboo & Tropea (2002),

---

† Current address Philips DAP, Tussendiepen, 4, 9200 CA Drachten, The Netherlands.

intended to predict the maximum extent of spreading that can be achieved under given impact conditions, by equating the initial (kinetic) energy of the droplet to the sum of the surface energy at maximum spreading and the energy dissipated during spreading. Simplifying assumptions with respect to the droplet shape (at maximum spreading frequently a circular disk shape is assumed) and the flow inside the droplet (such as a stagnation-point flow) are necessary in order to facilitate an estimation of the work done by the viscous forces. Also, the kinetic energy of the droplet at maximum spreading is considered to be zero. The resulting expression for the maximum diameter is found to give acceptable predictions only when $Re \gg 1$, $We \gg 1$ and θ is small. Park *et al.* (2003) changed the droplet shape assumption to a spherical cap to improve the predictions at low Re and We and large θ. Recently, Fedorchenko, Wang & Wang (2005) developed an analytical model, assuming a non-zero kinetic energy of droplet at maximum spreading, to describe the effects of capillary and viscous forces on initial and late stages of spreading. However, these analyses do not predict the outcome of impact.

Experimental work, mostly flash photography to visualize the impact of millimetre-size drops, has focused on the influence of surfactants (Pasandideh-Fard *et al.* 1996; Zhang & Basaran 1997; Crooks, Cooper-White & Boger 2001), viscoelasticity of the droplet material (Bergeron *et al.* 2000; Crooks & Boger 2001; Crooks, Cooper-White & Boger 2002), and surface roughness and wettability including superhydrophobicity of the solid (Range & Feuillebois 1998; Renardy *et al.* 2003). In addition, the effects of droplet diameter, impact velocity, viscosity and surface tension of the liquid as well as the influence of heat transfer with and without solidification (Zhao, Poulikakos & Fukai 1996*b*; Schiaffino & Sonin 1997; Bhola & Chandra 1999; Aziz & Chandra 2000) were also studied and outcomes classified as deposition, splash, rebound and partial rebound have been reported. However, only a few experimental studies exist on impact of micron-size droplets under conditions relevant to inkjet printing (Asai *et al.* 1993; Attinger, Zhao & Poulikakos 2000; van Dam & Clerc 2004). Asai *et al.* (1993) studied the impact of micron-size drops on different types of paper with the aim of developing a simple correlation between the maximum spreading and Re and We as an aid in designing inkjet printers. They found that the maximum spreading depends only on Re and We, irrespective of the paper characteristics. With solder-jetting for surface-mount technologies in mind, Attinger *et al.* (2000) investigated the effect of simultaneous flow and solidification on the impact of micron-size molten metal drops and found that the solidified droplet surface had ripples. Recently, van Dam & Clerc (2004) studied the impact of water droplets of 60 to 100 μm in diameter on a solid substrate having advancing and receding contact angles in the range of 15° to 70° and 0° to 5°, respectively. The parameter varied was the impact velocity, implying that both the Reynolds number and the Weber number were changed simultaneously. They observed differences in impact at $We \leqslant 1.1$ and $We \geqslant 8$ and concluded that this was due to the capillary force acting as driving force for spreading in the former cases. Resolving the time and length scales involved, typically about 100 μs and 100 μm, respectively, is experimentally difficult and therefore we adopt a supporting numerical approach to help find the relevant parameters and results of the process.

Numerical modelling of the droplet impact process should address: (i) tracking of the droplet–ambient fluid interface that undergoes extreme deformation in a short time and accounting for the surface tension, (ii) resolving the contact line singularity, and (iii) incorporating effects of the substrate wettability. Notwithstanding these complexities, a number of numerical studies have been reported (again) focusing on millimetre-size drops. Fukai *et al.* (1993) used a Lagrangian formulation implemented in a finite-element method in an axisymmetric framework neglecting wetting effects, which were accounted for in their subsequent work (Fukai *et al.* 1995). The contact line singularity was resolved by using a slip model (Dussan V. & Davis 1974). Later extensions by Zhao, Poulikakos & Fukai (1996*a*) and Attinger & Poulikakos (2001) of their model included heat transfer with solidification. This methodology requires frequent refinement of the mesh to cope with the large deformations experienced by the droplet in a short time and also it needs *ad hoc* rules to handle topological changes, such as breakup, when they occur. Concurrently, Pasandideh-Fard *et al.* (1996) used an Eulerian approach with a volume tracking 'fractional volume of fluid' method that captures the interface through a colour function C. The position and the shape of the interface that is required to account for the surface tension and contact angle is reconstructed from the values of C using some approximation such as a piecewise-linear interface construction. This interface reconstruction step may play an important role in the low-*We* cases considered here and also in handling topological transitions. Although they did not explicitly use any slip model, a mesh-dependent slip is inherently present, shown by Renardy, Renardy & Li (2001), in the marker-and-cell finite-difference method that was used to solve the system of equations. Subsequently, Bussmann, Mostaghimi & Chandra (1999) and Pasandideh-Fard *et al.* (2002) extended the method to three dimensions and included solidification. These earlier numerical studies neglected the dynamics of the gas phase and modelled only the liquid droplet phase treating it as a free-surface problem. Francois & Shyy (2003) used the immersed-boundary method to model the impact process as a two-phase flow problem. Recently, Šikalo *et al.* (2005) and Gunjal *et al.* (2005) applied the fractional volume-of-fluid method to model the effect of a dynamic contact angle on impact behaviour. Almost all of these studies were based on a classical sharp interface method.

In this paper, we use the Cahn–Hilliard diffuse-interface approach to model the impact of a micron-size liquid droplet on a perfectly smooth, chemically homogeneous solid surface. Our objective is to understand the impact process of micron-size droplets under conditions of low-to-moderate *We*, moderate *Re* and a wide range of contact angles. These conditions are prevalent in inkjet printing (of polymers) which is recently being explored as an alternative to photolithography in making patterned surfaces for electronics and various other applications (Sirringhaus *et al.* 2000; Okamoto, Suzuki & Yamamoto 2000; Kawase *et al.* 2003; de Gans, Duineveld & Schubert 2004).

Like the fractional volume-of-fluid method, the diffuse-interface model (DIM) also considers impact as a two-phase flow problem and is based on the idea that the fluid–fluid interface has a finite thickness over which various thermodynamic variables change continuously. Recently, the diffuse-interface model has been used to model a variety of physical phenomena, see for example, Anderson, McFadden & Wheeler (1998). However, it was first used by van der Waals (1893) to explain why equilibrium interfaces have surface tension, and, hence, DIM is endowed with capillarity. The thickness of the interface is closely related to the finite range of molecular interactions (Rowlinson & Widom 1989). The finite interaction range is represented by a non-local effect in the free energy: the local free-energy density depends not only on the local composition but also on the composition of the immediate environment (Davis & Scriven 1982). By using a mean-field approximation, the non-local effect in the free energy is represented by the dependence on the local composition gradients rather than on the non-local composition (Cahn & Hilliard 1958). This free energy determines both the interfacial thickness and the surface tension, that appears after coupling with the equations of motion as a distributed stress over the interfacial region. The position and the shape of the interface is a part of the solution – that is continuous throughout the system but may have large variations in the interfacial region – of the governing equations of DIM i.e. it captures the interface. The resolution of the contact line singularity is, in spite of applying a strict no-slip boundary condition, based on diffusion driven by the gradient in chemical potential, as was shown by the analyses performed by Seppecher (1996), Jacqmin (2000), Chen, Jasnow & Viñals (2000) and more recently by Briant, Wagner & Yeomans (2004) and Briant & Yeomans (2004). The diffuse-interface model can be extended to incorporate non-90° contact angles (a 90° contact angle appears 'naturally' in the model). Following Cahn (1977) and Jacqmin (2000) this has been achieved by postulating that the wall free energy which captures the wall–fluid interactions is dependent only on the composition at the wall. Recently Yarin *et al.* (2005) used a model similar to DIM to study the phase-change behaviour of fluids in nanochannels, including the wetting effects.

The paper is organized as follows: § 2 summarizes the model equations of DIM. Section 3 describes the system to which the equations of DIM are applied. Section 4 gives the boundary conditions imposed while § 5 deals with the numerical implementation of the governing equations. Results of droplet impact are presented and discussed in § 6. Finally, in § 7 some conclusions are drawn.

2. Model equations

The diffuse-interface model used is a two-phase model wherein the thermodynamics is coupled with the hydrodynamics and it is applied to a fluid, referred to as a binary fluid, consisting of two partially miscible components (Lowengrub & Truskinovsky 1998; Verschueren 1999). In the present case, one of the fluid components corresponds to the droplet whereas the other represents the ambient fluid. The individual components of the binary fluid have a constant density and viscosity, whereas the density and viscosity ratios between the components are typically of $O(10^3)$ and $O(10^2\text{–}10^3)$, respectively. The thermodynamic formulation to account for large density ratios results in a fairly complex, nonlinear model even when the flow is simplified using the Hele-Shaw approximation (Lee, Lowengrub & Goodman 2002*a*, *b*). In the current case, where inertia drives the flow, the complexity is likely to increase further. Hence to simplify the model we neglect the density difference in the thermodynamic formulation while retaining it in the hydrodynamic treatment. Such a simplification possibly results in the neglect of some quasi-incompressible effects and induces an error in the interfacial region, but can be rationalized by comparing the resulting simplified model with the classical sharp-interface model (Lowengrub & Truskinovsky 1998). Also, the simplified model is similar to the phase-field model used to study solidification of molten metal (Boettinger *et al.* 2002; Sekerka 2004).

The binary fluid is assumed to have a specific Helmholtz free energy which is based on the work of Cahn & Hilliard (1958):

$$f(c, \nabla c) = f_0(c) + \tfrac{1}{2}\epsilon|\nabla c|^2, \tag{2.1}$$

where c is the renormalized mass fraction of one of the components, f_0 is homogeneous part of the specific free energy and ϵ is the gradient-energy parameter. The homogeneous part f_0 is approximated by the so-called 'c^4' approximation

(Gunton, Miguel & Sahni 1983) also known as the Landau–Ginzburg free energy:

$$f_0(c) = \tfrac{1}{4}\beta c^4 - \tfrac{1}{2}\alpha c^2, \tag{2.2}$$

where α and β are both positive constants for an isothermal system below its critical temperature.

Combining (2.1) and (2.2), f can now be written as,

$$f = \tfrac{1}{4}\beta c^4 - \tfrac{1}{2}\alpha c^2 + \tfrac{1}{2}\epsilon|\nabla c|^2. \tag{2.3}$$

The chemical potential is defined as a variational derivative of the specific Helmholtz free energy (2.3) with respect to concentration and is

$$\mu = \frac{\delta f}{\delta c} = \beta c^3 - \alpha c - \epsilon\nabla^2 c. \tag{2.4}$$

For a planar interface (with z as the direction normal to the interface) at equilibrium, the corresponding concentration profile is given by

$$c(z) = c_B \tanh\left(\frac{z}{\sqrt{2}\xi}\right), \tag{2.5}$$

where $\xi = \sqrt{\epsilon/\alpha}$ is the interface thickness and $c_B = \pm\sqrt{\alpha/\beta}$ are the equilibrium bulk concentration. For example, $c_B = \sqrt{\alpha/\beta}$ corresponds to the droplet and $c_B = -\sqrt{\alpha/\beta}$ corresponds to the ambient fluid.

The interfacial tension γ_{lv} is defined as the excess free energy per unit surface area due to the inhomogeneity in c in the interfacial region (Rowlinson & Widom 1989):

$$\gamma_{lv} = \rho\epsilon \int_{-\infty}^{\infty} \left(\frac{\mathrm{d}c}{\mathrm{d}z}\right)^2 \mathrm{d}z. \tag{2.6}$$

Integrating (2.6) using the equilibrium concentration profile (2.5) yields

$$\gamma_{lv} = \frac{2\sqrt{2}}{3}\frac{\rho\epsilon c_B^2}{\xi}. \tag{2.7}$$

For mass conservation of individual components, the renormalized mass fraction c satisfies the local balance equation:

$$\frac{\partial c}{\partial t} + \boldsymbol{v}\cdot\nabla c = \nabla\cdot M\nabla\mu, \tag{2.8}$$

where M is the mobility, which in general can be a function of c. In the above equation, known as the convective Cahn–Hilliard equation, the diffusional flux is assumed to be proportional to the gradient in chemical potential. This equation without the convection term was originally used to describe the initial stages of spinodal decomposition (Cahn 1964).

Governing equations for the flow are obtained by coupling the momentum and total mass balance with the DIM equations, which yields a modified Navier–Stokes equation (Lowengrub & Truskinovsky 1998; Verschueren 1999):

$$\rho\left(\frac{\partial \boldsymbol{v}}{\partial t} + \boldsymbol{v}\cdot\nabla\boldsymbol{v}\right) = -\nabla p + \nabla\cdot\eta[(\nabla\boldsymbol{v}) + (\nabla\boldsymbol{v})^T] + \rho\,(\mu\nabla c - \nabla f) + \rho\boldsymbol{g}, \tag{2.9}$$

where p is the pressure, $\boldsymbol{v}$ is the barycentric velocity and $\boldsymbol{g}$ is the gravitational force per unit mass. The density of the binary fluid ρ, now considered to be a function of concentration c, is assumed to follow the simple mixture rule

(Joseph & Renardy 1993):

$$\frac{1}{\rho} = \frac{1}{\rho_d}\left(\frac{c+1}{2}\right) - \frac{1}{\rho_c}\left(\frac{c-1}{2}\right), \tag{2.10}$$

where ρ_d and ρ_c is the density of the droplet and ambient fluid, respectively. The viscosity η, is assumed to have the following linear relationship with the concentration c:

$$\eta = \eta_d\left(\frac{c+1}{2}\right) - \eta_c\left(\frac{c-1}{2}\right), \tag{2.11}$$

where η_d and η_c are the viscosities of the droplet and ambient fluid, respectively.

In the equation of continuity, the density ρ, is retained inside the divergence operation to give

$$(\nabla \cdot \rho \boldsymbol{v}) = 0. \tag{2.12}$$

2.1. *Non-dimensionalized equations*

The governing equations are non-dimensionalized using the following dimensionless variables:

$$c^* = \frac{c}{c_B};\quad \nabla^* = D_i\nabla;\quad \mu^* = \frac{\mu\xi^2}{\epsilon c_B};\quad f^* = \frac{f\xi^2}{\epsilon c_B^2};\quad \boldsymbol{v}^* = \frac{\boldsymbol{v}}{V_i};$$

$$t^* = \frac{tV_i}{D_i};\quad p^* = \frac{pD_i}{\eta_d V_i};\quad \boldsymbol{g}^* = \frac{\boldsymbol{g}}{g};\quad \eta^* = \frac{\eta}{\eta_d};\quad \rho^* = \frac{\rho}{\rho_d}.$$

The initial droplet diameter (D_i) and impact velocity (V_i) are used as the characteristic length and velocity scale, respectively.

The system of equations is, after dropping the asterisks,

$$\frac{\partial c}{\partial t} + \boldsymbol{v}\cdot\nabla c = \frac{1}{Pe}\nabla^2\mu, \tag{2.13}$$

$$\mu = c^3 - c - C_h^2\nabla^2 c, \tag{2.14}$$

$$f = \tfrac{1}{4}c^4 - \tfrac{1}{2}c^2 + \tfrac{1}{2}C_h^2|\nabla c|^2, \tag{2.15}$$

$$Re\,\rho\left(\frac{\partial \boldsymbol{v}}{\partial t} + \boldsymbol{v}\cdot\nabla\boldsymbol{v}\right) = -\nabla p + \nabla\cdot\eta[(\nabla\boldsymbol{v}) + (\nabla\boldsymbol{v})^T] + \frac{1}{CaC_h}\rho(\mu\nabla c - \nabla f) + \frac{Bo}{Ca}\rho\boldsymbol{g}, \tag{2.16}$$

$$\eta = \left(\frac{c+1}{2}\right) - \frac{1}{\lambda}\left(\frac{c-1}{2}\right), \tag{2.17}$$

$$\frac{1}{\rho} = \left(\frac{c+1}{2}\right) - \kappa\left(\frac{c-1}{2}\right), \tag{2.18}$$

$$(\nabla\cdot\rho\boldsymbol{v}) = 0. \tag{2.19}$$

The dimensionless groups that appear are: Péclet number Pe, Cahn number C_h, Reynolds number Re, capillary number Ca, Weber number We, Bond number Bo, density ratio κ and viscosity ratio λ, and are defined as

$$Pe = \frac{V_iD_i\xi^2}{M\epsilon};\quad C_h = \frac{\xi}{D_i};\quad Re = \frac{\rho_d V_i D_i}{\eta_d};\quad Ca = \frac{\eta_d V_i}{\gamma};$$

$$We = \frac{\rho_d V_i^2 D_i}{\gamma} = ReCa;\quad Bo = \frac{\rho_d D_i^2 g}{\gamma};\quad \kappa = \frac{\rho_d}{\rho_c};\quad \lambda = \frac{\eta_d}{\eta_c}.$$

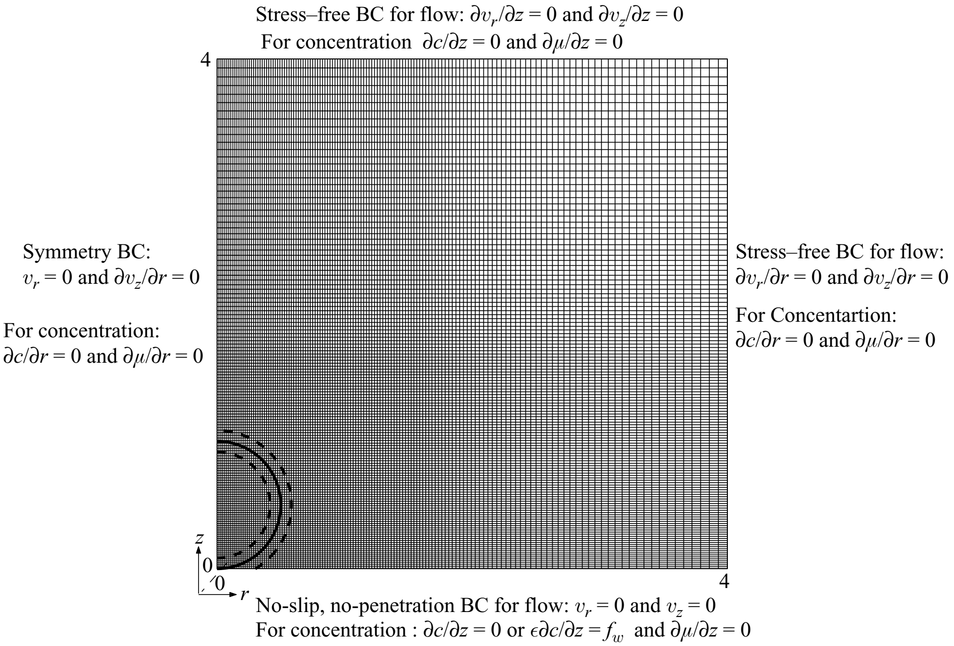

FIGURE 1. Computational domain, mesh, and initial and boundary conditions used for droplet spreading simulations. The dashed lines represent $c = \pm 0.9$ contours.

3. System definition

Consider the impact of a liquid droplet on a smooth, chemically homogeneous solid surface as shown in figure 1. Using axisymmetric coordinates and u and v to denote the radial and axial component of the velocity, respectively, the governing equations (2.13) – (2.19) take the following form:

$$\frac{\partial c}{\partial t} + u\frac{\partial c}{\partial r} + v\frac{\partial c}{\partial z} = \frac{1}{Pe}\left[\frac{1}{r}\frac{\partial}{\partial r}\left(r\frac{\partial \mu}{\partial r}\right) + \frac{\partial}{\partial z}\left(\frac{\partial \mu}{\partial z}\right)\right], \tag{3.1}$$

$$\mu = c^3 - c - C_h^2\left[\frac{1}{r}\frac{\partial}{\partial r}\left(r\frac{\partial c}{\partial r}\right) + \frac{\partial^2 c}{\partial z^2}\right], \tag{3.2}$$

$$f = \frac{c^4}{4} - \frac{c^2}{2} + C_h^2\left[\frac{\partial c}{\partial r}\frac{\partial c}{\partial r} + \frac{\partial c}{\partial z}\frac{\partial c}{\partial z}\right], \tag{3.3}$$

$$\begin{aligned} Re\,\rho\left(\frac{\partial u}{\partial t} + u\frac{\partial u}{\partial r} + v\frac{\partial u}{\partial z}\right) &= -\frac{\partial p}{\partial r} + \frac{1}{CaC_h}\rho\left(\mu\frac{\partial c}{\partial r} - \frac{\partial f}{\partial r}\right) \\ &\quad + \left[\frac{1}{r}\frac{\partial}{\partial r}\left(r2\eta\frac{\partial u}{\partial r}\right) - \frac{2\eta u}{r^2} + \frac{\partial}{\partial z}\left(\eta\left(\frac{\partial u}{\partial z} + \frac{\partial v}{\partial r}\right)\right)\right], \end{aligned} \tag{3.4}$$

$$\begin{aligned} Re\,\rho\left(\frac{\partial v}{\partial t} + u\frac{\partial v}{\partial r} + v\frac{\partial v}{\partial z}\right) &= -\frac{\partial p}{\partial z} + \frac{1}{CaC_h}\rho\left(\mu\frac{\partial c}{\partial z} - \frac{\partial f}{\partial z}\right) \\ &\quad + \left[\frac{1}{r}\frac{\partial}{\partial r}\left(r\eta\left(\frac{\partial u}{\partial z} + \frac{\partial v}{\partial r}\right)\right) + \frac{\partial}{\partial z}\left(2\eta\frac{\partial v}{\partial z}\right)\right] + \frac{Bo_i}{Ca}\left(\rho - \frac{1}{\kappa}\right), \end{aligned} \tag{3.5}$$

$$\frac{1}{r}\frac{\partial(\rho r u)}{\partial r} + \frac{\partial(\rho v)}{\partial z} = 0. \tag{3.6}$$

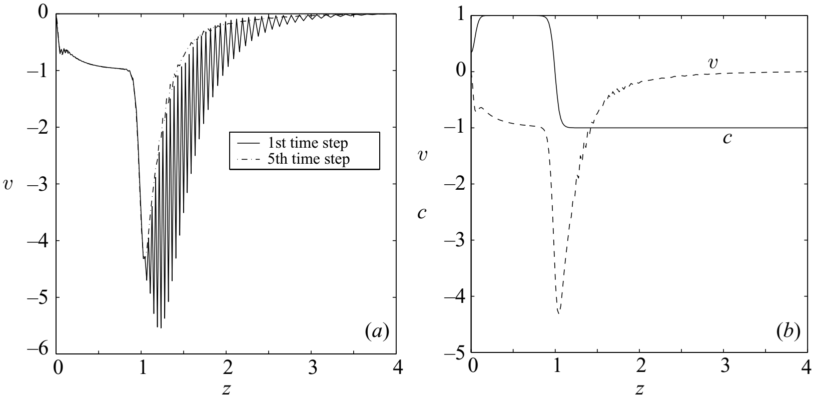

FIGURE 2. Comparison of (*a*) z-component of the velocity along the axis of symmetry after the first and the fifth time step and (*b*) concentration and z-component of the velocity along the axis of symmetry after the fifth time step. Simulation was performed with $C_h = 0.04$, $Pe = 2.5$, $Bo_i = 253\,000$, $Re = 13$, $We = 15$, $\lambda = 1000$, $\kappa = 10$, $\theta = 90^\circ$ and $\Delta t = 10^{-4}$ on a mesh consisting of 4900 second-order elements.

Note that for the impact of micron-size droplets considered in this paper, the effect of gravity is negligibly small; typically $Bo = 10^{-3}$. The gravitational force is therefore set equal to zero except for the first time step. At the first time step, as described later in § 4.1, an artificial value of the gravitational force number is prescribed via the Bond to impart the desired impact velocity to the droplet. The gravity term in (2.9), (2.16) and (3.5) is retained to depict a general impact scenario whereas Bo is replaced by Bo_i in (3.5) to reflect the artificial nature of the gravitational force. Equations (3.1)–(3.6) are supplemented with the initial and boundary conditions as described in the next section.

4. Initial and boundary conditions

4.1. *Specifying the initial (impact) velocity field*

The diffuse-interface approach involves at least two fluids/phases, the droplet and the ambient fluid in the present case. Because of the hydrodynamic coupling between the two phases, it is not possible in DIM to specify the initial velocity as is done in the sharp-interface approach where inside the droplet a velocity equal to the impact velocity and zero outside is specified. The proof of this is given in Appendix A.

A method to overcome this difficulty is to exploit the density difference between the droplet and the ambient fluid. A large body force (gravity) is applied on an initially stationary droplet just for one time step. The body force, prescribed in terms of an artificial Bond number whose value is estimated roughly as shown in Appendix B, is such that it gives a non-dimensional velocity of −1 inside the droplet. Figure 2 shows the z-component of the velocity along the symmetry axis of the droplet as a function of z obtained with $Bo_i = 253\,000$, $We = 15$, $Re = 13$, $\Delta t = 10^{-4}$ and $\kappa = 10$. Also, the concentration along the symmetry line is plotted. The velocity immediately after the first time step is oscillatory due to the sudden nature of accelerating the droplet from rest to the impact velocity. The oscillations, however, dampen quickly in about five time steps. As desired, for $c = +1$ which corresponds to the droplet, $v \approx -1$ and as c changes from $+1$ to -1 v goes from -1 to -4. Such an increase in v is also predicted by equation (A 3).

This method to specify the impact velocity by applying a large body force only for one time step is used in all the droplet impact simulations reported in this study.

4.2. *Initial concentration field*

The initial concentration field is specified using the equilibrium solution corresponding to the droplet in an infinite domain of ambient fluid. The specification is such that the contour $c = 0$, which is considered to represent the droplet–ambient-fluid interface, just touches the solid wall at $z = 0$.

4.3. *Partial wetting boundary conditions*

The wall, i.e. the solid surface at $z = 0$, may be neutral or may be preferentially wetted by one of the components of the binary fluid. This effect is accounted for by following the approach given in Cahn (1977) where solid–fluid interactions are assumed to be short-ranged. By this assumption, the total system free energy $\mathscr{F}$ can be written as

$$\mathscr{F} = \int_{\Omega} f \, \mathrm{d}\Omega + \int_{\Gamma} f_w \, \mathrm{d}\Gamma, \tag{4.1}$$

where f_w is the specific wall free energy which depends only on the concentration at the wall and Ω is the domain volume bounded with a wall of surface Γ. The surface integral term in (4.1) represents the contribution of solid–fluid interactions.

At equilibrium, $\mathscr{F}$ is at its minimum. Minimizing $\mathscr{F}$ using methods of variational calculus subject to natural boundary conditions (Beveridge & Schechter 1970) gives the following boundary condition on surface Γ:

$$-\epsilon \frac{\partial c}{\partial n} + \frac{\partial f_w}{\partial c} = 0, \tag{4.2}$$

where n is the direction normal to Γ.

For f_w we use the form proposed by Jacqmin (2000):

$$f_w = \phi \left(c - \frac{c^3}{3} \right), \tag{4.3}$$

where ϕ is assumed to be a constant and referred to as the wetting potential. It can be made to vary spatially to indicate chemical heterogeneity of the solid surface. With f_w of the form (4.3), $\partial f_w / \partial c$ evaluated at c_B is zero, so at equilibrium the wall is not enriched in one of the fluids and depleted in the other. Surface enrichment effects are of interest when considering critical wetting (de Gennes 1985). In the present study we do not consider such complicated effects and therefore restrict to the case where no wall layer exists at equilibrium.

Equations (4.2) and (4.3) are non-dimensionalized using the dimensionless variables defined in §2.1 with the addition of γ_{lv} as the characteristic scale for the specific wall free energy to give

$$-C_h \frac{\partial c}{\partial n} + \Phi(1 - c^2) = 0, \tag{4.4}$$

$$f_w = \Phi \left(c - \frac{c^3}{3} \right), \tag{4.5}$$

where $\Phi = \phi c_B / \gamma_{lv}$ is the dimensionless wetting potential.

Using Young's equation which connects the contact angle with the surface and interfacial tensions of the liquid (γ_{lv}) and the solid (γ_{sv}, γ_{sl}),

$$\cos\theta = \frac{\gamma_{sv} - \gamma_{sl}}{\gamma_{lv}}, \tag{4.6}$$

Φ can be related to the (equilibrium) contact angle θ to yield

$$\cos\theta = \tfrac{4}{3}\Phi. \tag{4.7}$$

From (4.7) it is concluded that for a contact angle θ equal to 90°, Φ is zero and the mixed boundary condition (4.4) reduces to a natural boundary condition. We have applied the above boundary condition (4.4) assuming that the wall at $z = 0$ is at local equilibrium.

A related issue is the existence of the advancing and receding contact angles that usually have different values and depend on the velocity of the contact line. However, this dependence has been studied only for slow, about a few $\mathrm{mm\,s^{-1}}$, contact line speeds. The contact line speed in droplet impact problems is considerable and can reach values higher than the impact velocity (Fukai *et al.* 1993). Owing to the lack of experimental data on the advancing and receding contact angles, some previous researchers either used constant (but different) values for the advancing and receding contact angles (Fukai *et al.* 1995) or gave experimentally measured (by themselves) variations of the contact angle with time as an input to their model (Pasandideh-Fard *et al.* 1996). Here, for simplicity (as the experimental determination of the dependence of the advancing and receding contact angles on the contact line velocity is difficult and ambiguous (Blake 1993)), we assume that the advancing and receding contact angles are constant and equal to each other. Note, however, that the DIM applied can be straightforwardly extended to take these effects into account, for example, by making the wetting potential Φ a function of the contact line velocity.

4.4. *Flow boundary conditions at the solid surface*

From the analysis of Huh & Scriven (1971) it is well-known that the application of a no-slip boundary condition for a moving contact line using a classical, sharp-interface approach leads to a stress singularity. To overcome this problem, various models have been proposed; prominent among them are slip models (Dussan V. & Davis 1974; Hocking 1977; de Gennes 1985). In the diffuse-interface model, the contact line moves via diffusion driven by the chemical-potential gradient as shown by Seppecher (1996), Jacqmin (2000) and Chen *et al.* (2000). Hence, we apply a no-slip, no-penetration boundary condition at the solid surface:

$$\boldsymbol{v} = \boldsymbol{0}. \tag{4.8}$$

Other boundary condition used is (shown in figure 1): no-mass-flux condition for the chemical potential

$$\nabla\mu\cdot\boldsymbol{n} = 0, \tag{4.9}$$

where $\boldsymbol{n}$ is the unit normal vector to the boundary.

5. Numerical method

Instead of solving the full system (3.1)–(3.6) for c, μ, u, v and p, we decouple the set into a flow problem (3.3)–(3.6) and a concentration problem (3.1)–(3.2).

The flow problem is solved using primitive variables, i.e. a velocity–pressure formulation, and spatially discretized by a standard Galerkin finite-element method. Crouziex–Raviart quadrilateral elements, with discontinuous pressure, that employ a biquadratic approximation for velocity and a bilinear approximation for pressure, are used. The time derivative in (3.4) and (3.5) is approximated by a first-order Euler implicit method. The nonlinear convective term $\boldsymbol{v}\cdot\nabla\boldsymbol{v}$ is linearized to $\boldsymbol{v}^{n-1}\cdot\nabla\boldsymbol{v}^{n}$, with

n denoting the current time level, using Picard's method of successive substitution. The discretized equations written in matrix form are,

$$\begin{bmatrix} Re\,\rho^{n-1}\left\{\boldsymbol{M}+\Delta t\left(\boldsymbol{N}_v^{n-1}-\boldsymbol{S}_v\right)\right\} & \Delta t\,\boldsymbol{L}^T \\ \boldsymbol{L} & \boldsymbol{0} \end{bmatrix} \begin{bmatrix} \boldsymbol{v} \\ p \end{bmatrix} = \begin{bmatrix} \boldsymbol{M}\boldsymbol{v}^{n-1}+\Delta t\,\boldsymbol{M}\boldsymbol{f}_v \\ \boldsymbol{0} \end{bmatrix}, \tag{5.1}$$

where $\boldsymbol{v}$ is the discretized velocity, p is the discretized pressure, Δt is the time step, $\boldsymbol{M}$ is the mass matrix, $\boldsymbol{N}_v$ is the convection matrix, $\boldsymbol{S}_v$ is the stiffness matrix containing the viscous terms, $\boldsymbol{L}$ is the matrix due to divergence operation, $\boldsymbol{L}^T$ is the matrix for the gradient operation and $\boldsymbol{f}_v$ is the right-hand side containing the $\rho(\mu\nabla c-\nabla f)/Ca\,C_h$ term. At the first time step $\boldsymbol{f}_v$ also contains the body force term: (Bo_i/Ca) $(\rho-1/\kappa)$.

The discretized set (5.1) of linear algebraic equations is solved using an integrated method, with an iterative (conjugate gradients square) solver with incomplete Cholesky decomposition as a preconditioner. In the integrated method (Segal 1995), both the velocity and the pressure are used as unknowns, i.e. degrees of freedom. Owing to the absence of pressure in the continuity equation, a zero block appears in the main diagonal of the matrix. It is therefore possible that the first pivot during the elimination process for the ILU preconditioner is zero. In order to ensure that this does not happen, unknowns are renumbered per level and, also, globally so that first velocities and then the pressure unknowns are used during the matrix assembling.

Two second-order differential equations (3.1) and (3.2) that constitute the concentration problem are solved in a coupled way. For temporal discretization of (3.1) a first-order Euler implicit scheme is employed so that the discretized time derivative is $(c^n-c^{n-1})/\Delta t$ where Δt is the time step size; superscript n represents the current time level. The nonlinear c^3 term in equation (3.2) is linearized by a standard Picard iteration which yields $(c_{i-1}^n)^2 c_i^n$ where subscript i represents the ith Picard iteration at time level n.

For spatial discretization of the set of equations a spectral-element method (Patera 1984; Timmermans, van de Vosse & Minev 1994) is used. In this method, similar to the finite-element method, the computational domain is divided into N_{el} non-overlapping sub-domains Ω_e and a spectral approximation is applied on each element. The basis functions, $\hat{\phi}$, that are used for spatial discretization, are high-order Lagrange interpolation polynomials through Gauss–Lobatto integration points defined per element. In the present study, however, the spectral order of approximation was restricted to two. This restriction ensures that the finite-element mesh and the spectral-element mesh used to discretize the flow problem and the concentration problem, respectively, are identical. This eliminates any error that may be introduced when interpolating the velocity from the finite-element mesh to the spectral-element mesh and vice versa with the concentration. The higher-order (>2) spectral approximation is useful when solving the flow problem in a stream-function–vorticity formulation (Verschueren, van de Vosse & Meijer 2000; Keestra *et al.* 2003). For the problem investigated in this paper, the flow problem is better solved in primitive variables, i.e. using a velocity–pressure formulation as the boundary conditions for the velocity can be prescribed (Anderson, Keestra & Hulsen 2006).

The weak form in the present axisymmetric case is derived following the approaches of Gerritsma & Phillips (2000) and Fournier *et al.* (2004) where the cylindrical radius appearing in the definition of the infinitesimal volume element is incorporated into the weighting function. This is done to circumvent '0=0' trivial solutions which may arise due to application of Gauss–Lobatto–Legendre to axisymmetric problems in the limit of $r = 0$. The resulting set of discretized equations written in matrix form is

$$\begin{bmatrix} \boldsymbol{M} + \Delta t \tilde{\boldsymbol{N}}_c^n & \dfrac{\Delta t}{Pe}(\tilde{\boldsymbol{S}}_\mu - \tilde{\boldsymbol{N}}_{\mu c}) \\ \left[1 - \left(c_{i-1}^n\right)^2\right]\boldsymbol{M} + 2\Phi C_h c_{i-1}^n \boldsymbol{M}_{BC} - C_h^2(\tilde{\boldsymbol{S}}_c - \tilde{\boldsymbol{N}}_{c\mu}) & \boldsymbol{M} \end{bmatrix} \begin{bmatrix} c_i^n \\ \mu_i^n \end{bmatrix} = \begin{bmatrix} \boldsymbol{M} c_0^{n-1} \\ \Phi C_h \left[1 + \left(c_{i-1}^n\right)^2\right]\boldsymbol{M}_{BC} \end{bmatrix}, \qquad (5.2)$$

where c_i^n is discretized concentration at the ith Picard iteration at time step n, μ_i^n is discretized chemical potential at the ith Picard iteration at time step n, c^{n-1} is discretized concentration at time step $n-1$, $\boldsymbol{M}$ is the mass matrix, $\tilde{\boldsymbol{N}}_c$ is the convection matrix, $\tilde{\boldsymbol{S}}_\mu$ is the Cartesian diffusion matrix operating on μ, $\boldsymbol{M}_{BC}$ is the mass matrix arising through the linearization of boundary condition (4.4) and $\tilde{\boldsymbol{S}}_c$ is the Cartesian diffusion matrix operating on c. $\tilde{\boldsymbol{N}}_{c\mu}$ and $\tilde{\boldsymbol{N}}_{\mu c}$ are convection-like matrices resulting from the description in axisymmetric coordinates and operating on c and μ, respectively. These convection-like terms have $1/r$ as a ‘radial velocity’ while the ‘axial velocity’ is zero in both cases. Should these convection-like terms be evaluated at $r = 0$ while performing element integrals using Gauss–Lobatto–Legendre integration, they would create numerical problems. To avoid this, a small factor δ is added to r. The value of δ was chosen to be 10^{-3}. This value was used since identical results were obtained with $\delta = 10^{-3}$ and 10^{-6}. The discretized set (5.2) is also solved using the previously mentioned iterative solver.

The scheme to advance in time is as follows:

Step 1. Given the initial concentration profile c_0^0 and the initial velocity field $\boldsymbol{v}^0$, compute f, μ, ρ and η.

Step 2. Solve the system (5.1) for velocity ($\boldsymbol{v}^1$) with terms containing concentration treated explicitly.

Step 3. Solve the system (5.2) iteratively for concentration (c^1) and chemical potential (μ^1). Iterations are required due to the nonlinear term. Iteration is started with $c_1^1 = c^0$ and stopped when $\max |c_i^1 - c_{i-1}^1| \leqslant \delta_c$. The tolerance, δ_c, is set equal to 10^{-6}.

Step 4. Update the time and repeat steps 2–4.

The numerical scheme described above is implemented in SEPRAN (Segal 1995), a general finite-element package used for simulating droplet impact on a computational domain spanning a dimensionless length of 4 in both the radial and axial directions as shown in figure 1.

6. Results and discussion

Numerical results for droplet impact, more precisely for the spreading that ensues just after a droplet hits a solid surface, under conditions similar to inkjet printing, obtained using DIM are presented here. The results cover the range of values of the Reynolds number Re: 1.5 to 130, the Weber number We: 0.15 to 150 and the contact angle θ: 45° to 135°. For this parametric range, the impact can still be described in an axisymmetric framework (Kim, Park & Min 2003; van Dam & Clerc 2004). All the results reported here were obtained with a fixed value of 0.04 for the Cahn number C_h and a fixed value of 10 for the density ratio between the droplet the ambient fluid. The interface thickness for a simple liquid-liquid system is typically about a few nanometres. This means that C_h is about 10^{-3} as the droplet sizes studied here are about tens of microns. Such a small value of C_h is, however, computationally prohibitive to use and hence $C_h = 0.04$ was chosen for numerical convenience, as has become customary (Chella & Viñals 1996; Jasnow & Viñals 1996; Jacqmin 1999; Verschueren *et al.* 2000; Keestra *et al.* 2003; Yue *et al.* 2004; Khatavkar, Anderson & Meijer 2006). Note that adaptive meshing such as in Barosan, Anderson & Meijer (2006) can be implemented in an attempt to capture the real value of C_h, but this is beyond the scope of the present work. The use of numerically wide interfaces exacerbates the curvature-dependent solubility inherent in DIM as it is proportional to the interface thickness, see for example Jacqmin (1999) and Naumann & He (2001). In view of the values used for the density ratio and the Cahn number the system modelled here can be best considered as one where the ambient fluid is a liquid having some inertia rather than an inertialess gas. As mentioned earlier in § 2, the thermodynamic formulation to account for large density ratios results in a fairly complex nonlinear model even when the flow is simplified using the Hele-Shaw approximation (Lee *et al.* 2002*a*,*b*). In addition to (renormalized) mass fraction, it may be necessary to include a squared gradient contribution of the density to the free energy (2.1) (Jasnow & Viñals 1996). In the current case, where inertia drives the flow, the complexity is likely to increase further. Hence to simplify the model we neglect the density difference in the thermodynamic formulation while retaining it in the hydrodynamic treatment.

Also, other than in § 6.8 where the effect of the Péclet number is considered, a fixed Péclet number of 2.5 was used. This means that when the initial droplet diameter or impact velocity are varied, rather than fixing the absolute values of the interface thickness and the mobility, the ratio of interface thickness to initial droplet diameter and the relative importance of convection to diffusion are kept constant. Most of the computations were performed with a time step of 10^{-4} on a graded mesh, as shown in figure 1, comprising about 4900 second-order elements, though in some cases, for example to establish time-step and mesh independence of the results, a time step of 5×10^{-4} and a mesh of 8100 elements has also been employed. A typical run with a time step of 10^{-4} on a mesh of 4900 elements takes about 2–3 min to advance one step in time.

First, impact under conditions that yield markedly different outcomes are described which demonstrate the capability of DIM to handle topological transitions. The resolution of other important issues related to the droplet spreading have been studied among others by Seppecher (1996), Jacqmin (2000) and recently by Khatavkar, Anderson & Meijer (2007) who show that the capillary spreading of a diffuse droplet tends to approach the classical sharp-interface results in the limit of zero contact angle. Next, the influence of individual parameters, such as droplet diameter, impact velocity, surface tension, droplet viscosity, the contact angle, etc. on the impact process is given. The results are then mainly presented as a plot of the spread factor, defined as the ratio of the diameter of the wetted surface area, i.e. the contact diameter of the droplet with the solid surface, to the initial droplet diameter and given by the position where $c = 0$ contour intersects with the solid surface at $z = 0$, versus the dimensionless time.

6.1. *Pedot droplet*

We start with the description of a 67 μm diameter droplet impacting with a velocity of $4\,\mathrm{m\,s^{-1}}$ on a smooth, chemically homogeneous solid surface. The droplet material is assumed to have a dynamic viscosity of 0.02 Pa s, surface tension with the ambient

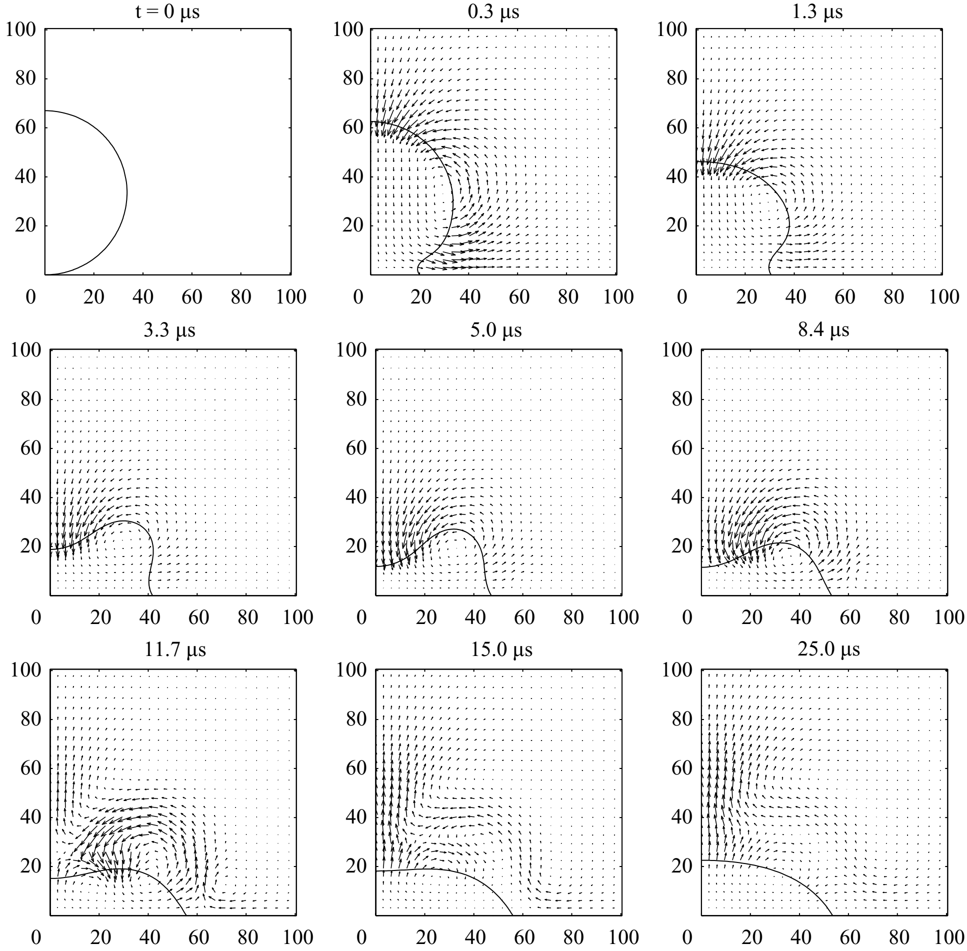

FIGURE 3. Droplet shapes with the corresponding velocity field at different times during spreading obtained for a Pedot droplet of diameter of 67 μm impacting with a velocity of 4 m s^{-1} on a flat solid surface. Simulation was performed with $C_h = 0.04$, $Pe = 2.5$, $Re = 13$, $We = 15$, $\lambda = 1000$, $\theta = 60^\circ$ and $\Delta t = 10^{-4}$ on a mesh consisting of 4900 second-order elements.

fluid of 0.07 N m^{-1} and a fixed contact angle of 60° with the solid surface. These conditions are representative of jetting a droplet of aqueous Pedot solution in air onto a photoresist surface (Duineveld 2003). The viscosity ratio between the droplet and the ambient fluid is taken to be 1000, which is close to the actual value of 1100 for a droplet of aqueous Pedot solution in air. The above conditions yield the following values for the dimensionless groups: $Re = 13$, $We = 15$ and $Ca = 1.15$. Owing to the initial impact energy possessed by the droplet, it begins to spread and deform in shape, with a very small foot at the base that can be seen in figure 3, for example at $t = 0.3$ μs. Until the early stage of spreading, i.e. $t \approx 2.5$ μs, the maximum splat height is at the axis of symmetry of the droplet. After this time, the maximum splat height is the height of the ring that forms at the periphery of the droplet due to a faster decrease in the height of the droplet at the axis of symmetry than the corresponding increase of the droplet base radius. At some point in time the impact energy falls, partly due to dissipation as viscous work and partly due to storage as surface energy,

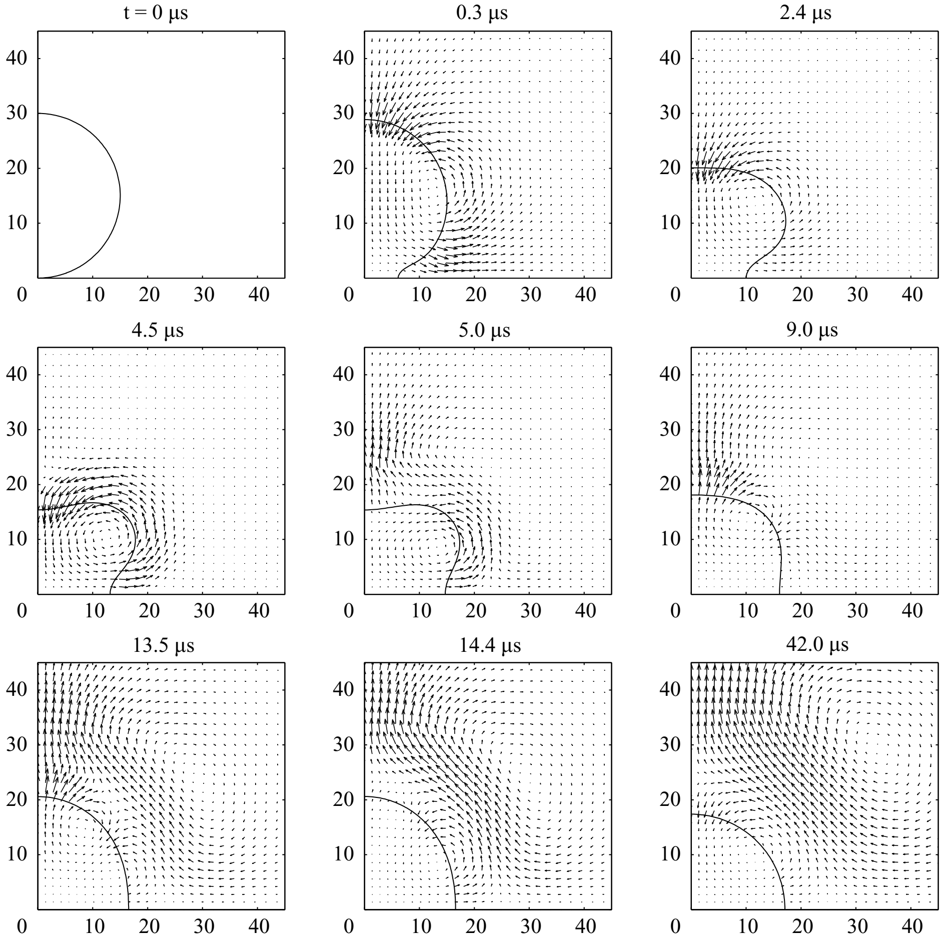

FIGURE 4. Droplet shapes with the corresponding velocity field at different times during spreading obtained for a Pedot droplet of diameter of 30 μm impacting with a velocity of $1\,\mathrm{m\,s^{-1}}$ on a flat solid surface. Simulation was performed with $C_h = 0.04$, $Pe = 2.5$, $Re = 1.5$, $We = 0.43$, $\lambda = 1000$, $\theta = 90°$ and $\Delta t = 10^{-4}$ on a mesh consisting of 4900 second-order elements.

to such a level that the height at the axis of symmetry reaches a minimum. The droplet apex at the axis of symmetry then starts to retract while the droplet base still continues to spread, albeit with a decreasing speed. The liquid in the ring flows to meet these demands, with the apparent generation of a vortex as seen, for example at $t = 11.7$ μs. Consequently, the ring diminishes in size. At about $t = 14$ μs, the droplet base spreads to a maximum extent. Beyond this time, the entire droplet recoils to attain the equilibrium shape.

Next, we consider the impact of a 30 μm diameter droplet with a velocity of $1\,\mathrm{m\,s^{-1}}$. The solid surface is assumed to be equally wetted by the droplet and the ambient fluid, so the contact angle is 90°. Keeping the other parameters the same as above, the dimensionless groups Re, We and Ca now have values of 1.5, 0.43 and 0.29, respectively. In this case, as shown in figure 4, the droplet starts to spread without a foot as the contact angle is 90°. Also, since $Re \approx 1$ and $We < 1$, the resisting viscous and surface forces are more dominant than the inertia compared to the previous

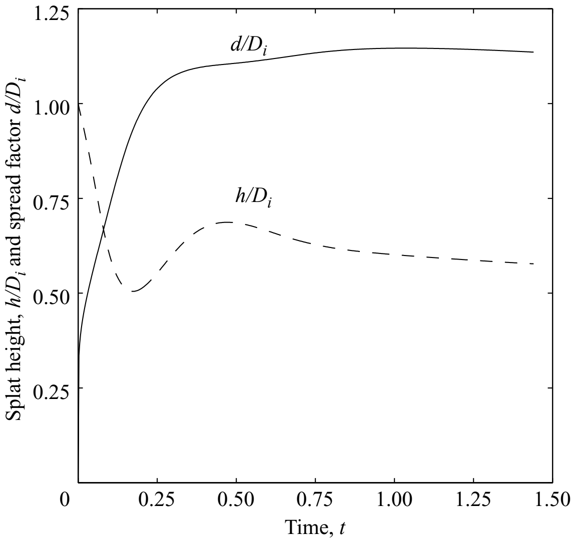

FIGURE 5. Spread factor versus time corresponding to figure 4.

case. Consequently, the droplet deforms to a lesser extent and no ring is formed. At $t = 5.2\,\mu s$ the droplet apex attains a minimum and thereafter retracts under the action of surface tension. But, the retraction is greater than the equilibrium value. So, the droplet apex, after reaching a maximum at $t = 14\,\mu s$ moves downward again. During all this time, the droplet base spreads without recoiling. On a plot of spread factor versus time, see figure 5, a drastic change in the slope can be seen at a dimensionless time $t = 0.5(15\,\mu s)$ which is probably due to the shift from inertia to capillary spreading of the droplet base.

Finally, figure 6 shows the time sequence of the impact of a 157 μm diameter Pedot droplet with a velocity of $0.83\,m\,s^{-1}$ on a hydrophobic surface characterized by a contact angle of 135°. The viscosity of the droplet in this case is taken to be 0.01 Pa s while the surface tension is kept the same as before. The values of Re, We, Ca and λ are therefore 13, 1.5, 0.115 and 1000, respectively. Owing to the large contact angle the droplet has with the solid, it spreads a maximum of only 1.1 times its initial diameter. Also, as the viscous force is about 10 times smaller than the inertial force, most of the initial impact energy, apart from that dissipated in deforming the droplet, is stored as surface energy. As a consequence, the droplet recoils intensely and at $t \approx 220\,\mu s$ lifts off entirely from the solid surface with a top-heavy shape similar to that shown in Renardy *et al.* (2003) for mm size droplets.

6.2. *Water droplet*

Now, we consider impact of a 157 μm water droplet with a velocity of $0.83\,m\,s^{-1}$, with Re, We, Ca and λ of 130, 1.5, 0.0115, and 100, respectively. This is an example where inertial and surface forces are nearly equal to each other but are larger than the viscous forces. The spreading process is such that at $t \approx 28\,\mu s$ the droplet apex at the axis of symmetry ceases to be maximum and a ring begins to form at the droplet periphery. The central liquid film, seen in figure 7 at $t = 51.8\,\mu s$ and connected with the ring, ruptures at $t = 57\,\mu s$ creating a toroidal droplet with a central dry-out. Occurrence of a toroidal droplet with a central dry-out was recently reported by Renardy *et al.* (2003) for droplets of millimetre size. They also presented a numerical

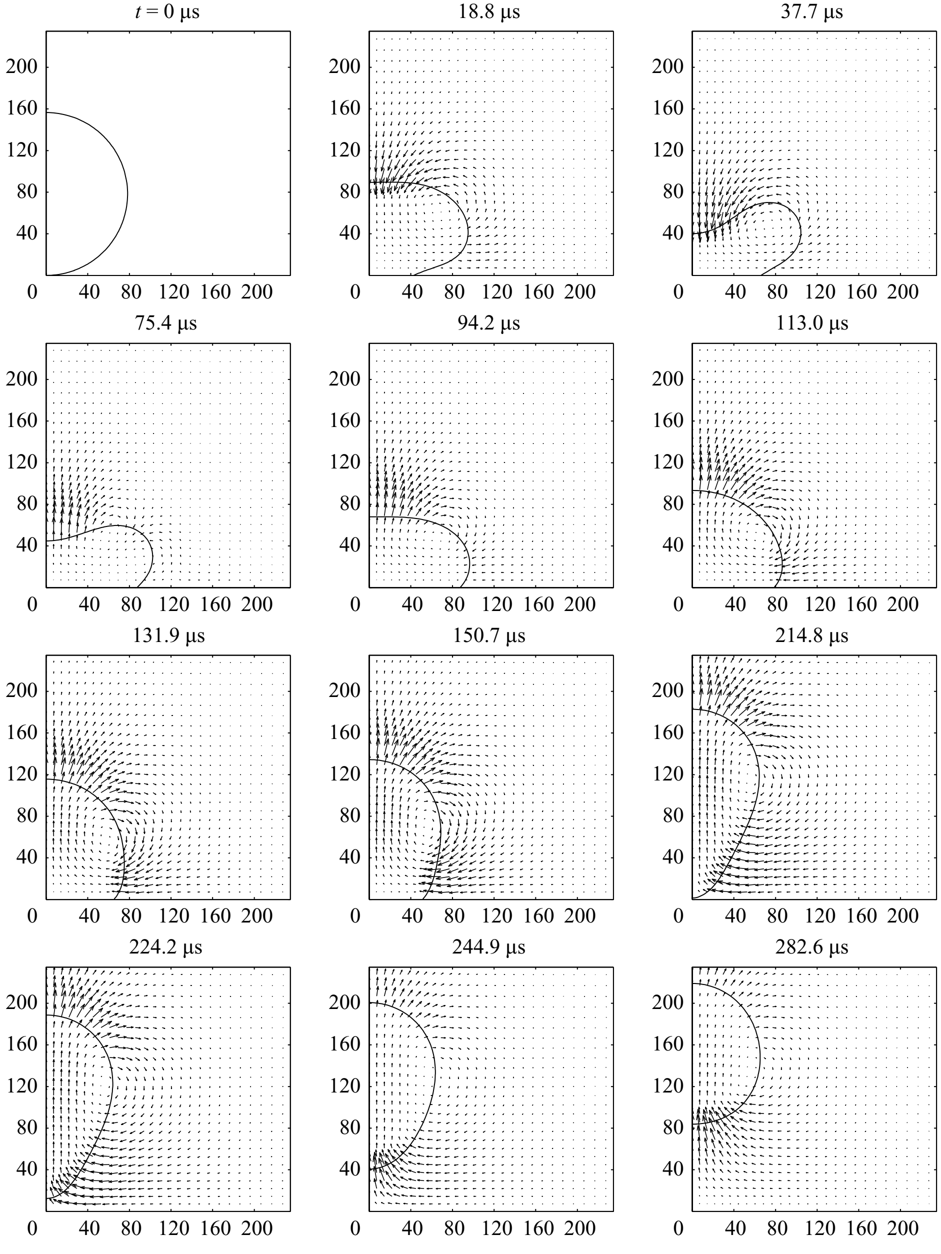

FIGURE 6. Droplet shapes with the corresponding velocity field at different times during spreading obtained for a Pedot droplet of diameter of 157 μm impacting with a velocity of $0.83\,\mathrm{m\,s^{-1}}$ on a flat solid surface. Simulation was performed with $C_h = 0.04$, $Pe = 2.5$, $Re = 13$, $We = 1.5$, $\lambda = 1000$, $\theta = 135°$ and $\Delta t = 10^{-4}$ on a mesh consisting of 4900 second-order elements.

curve delineating critical values of We and Re for which the droplet becomes a torus after impact. According to that curve a toroidal droplet could not form at the present values $We = 1.5$ and $Re = 13$. A reason for this may be related to the values of Pe and C_h used in the present study as briefly discussed further on in § 6.8. The droplet with a torus shape spreads until $t = 179$ μs at which maximum spreading is reached

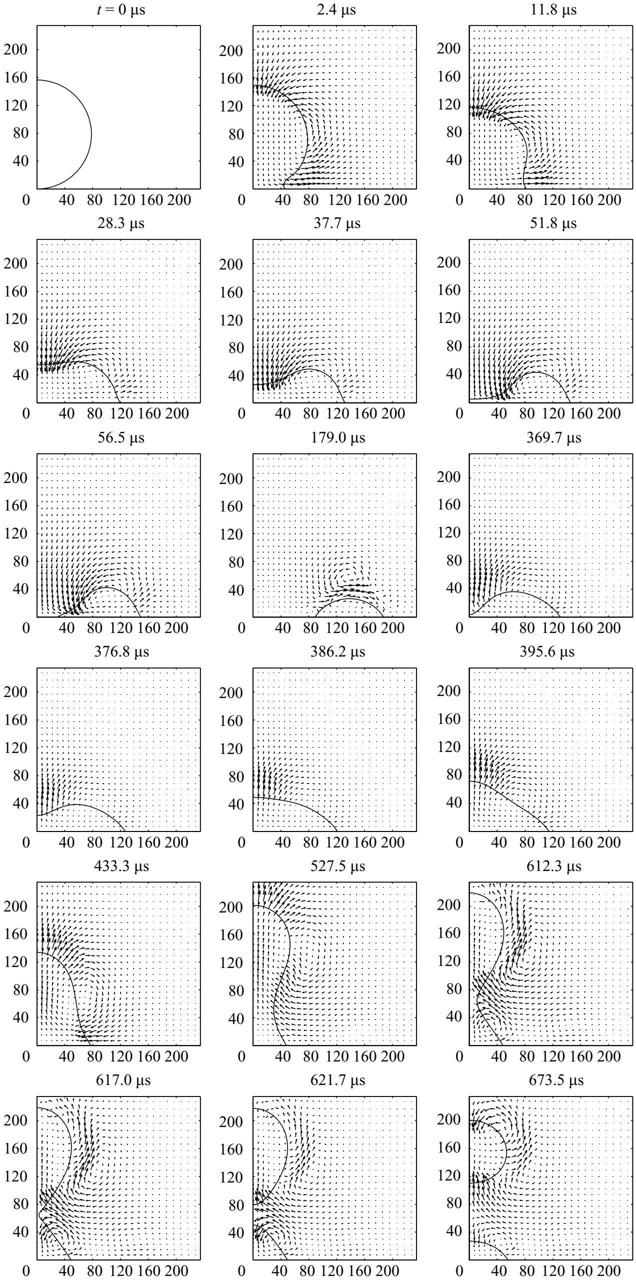

FIGURE 7. Droplet shapes with the corresponding velocity field at different times during spreading obtained for a water droplet of diameter of 157 μm impacting with a velocity of $0.83\,\mathrm{m\,s^{-1}}$ on a flat solid surface. Simulation was performed with $C_h = 0.04$, $Pe = 2.5$, $Re = 130$, $We = 1.5$, $\lambda = 100$, $\theta = 60°$ and $\Delta t = 5 \times 10^{-4}$ on a mesh consisting of 4900 second-order elements.

and thereafter it recoils with a continuous decrease in the surface area of the dry-out region. At $t \approx 369$ μs the dry-out region completely vanishes due to confluence of the inner, receding edge of the toroidal droplet. Owing to the moderately high value of *Re* and low value of *We*, most of the impact energy is stored as surface energy which leads

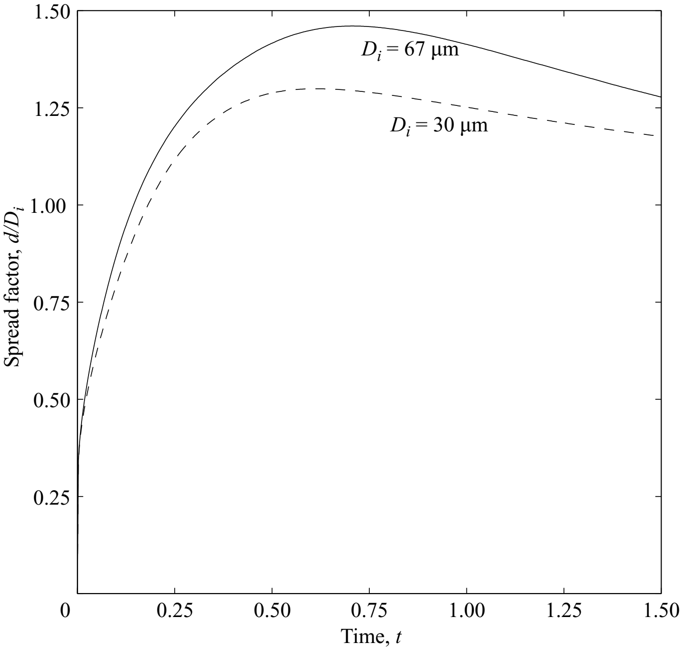

FIGURE 8. Effect of the initial droplet diameter on a Pedot droplet impacting at a velocity of 4 m s^{-1}. Other simulation parameters: $C_h = 0.04$, $Pe = 2.5$, $\lambda = 1000$, $\theta = 90°$ and $\Delta t = 1 \times 10^{-4}$ on a mesh consisting of 4900 second-order elements.

to recoil intense enough to result in a partial rebound of the droplet, i.e. the droplet breaks up into two parts. The detached larger part of the droplet does not possess sufficient energy to fly off and, since gravity is neglected, it does not fall back onto the smaller part that remains in contact with the solid surface. It relaxes to a spherical shape and starts to dissolve into the ambient fluid owing to the solubility inherent in the c^4 description of the free energy (Naumann & He 2001; Keestra *et al.* 2003).

6.3. *Effect of initial droplet diameter*

Figure 8 shows the effect of varying the initial droplet diameter while other parameters are held constant, on a plot of the spread factor versus the dimensionless time. The larger droplet ($Re = 13$) spreads more than the smaller droplet ($Re \approx 6$) owing to higher impact energy relative to the resisting viscous work. But, on roughly doubling of the initial droplet diameter the maximum spread factor increases only by 12%. Also, the time at which maximum spread factor is reached increases with the initial droplet diameter.

6.4. *Effect of impact velocity*

The influence of varying the impact velocity on impact of a 30 μm Pedot droplet is shown in figure 9. Similarly to increasing the initial droplet diameter, increasing the impact velocity increases the maximum extent of spreading. The dimensionless time required to attain the maximum spreading shows a non-monotonic behaviour, decreasing first as the impact velocity increases from 1 to 4 m s^{-1} and increasing afterwards. This is because at $Re \approx 1$ for impact velocity of 1 m s^{-1} the spread factor does not overshoot the equilibrium value. Nonetheless, the dimensional time required to approach the maximum extent of spreading decreases monotonically with increasing impact velocity.

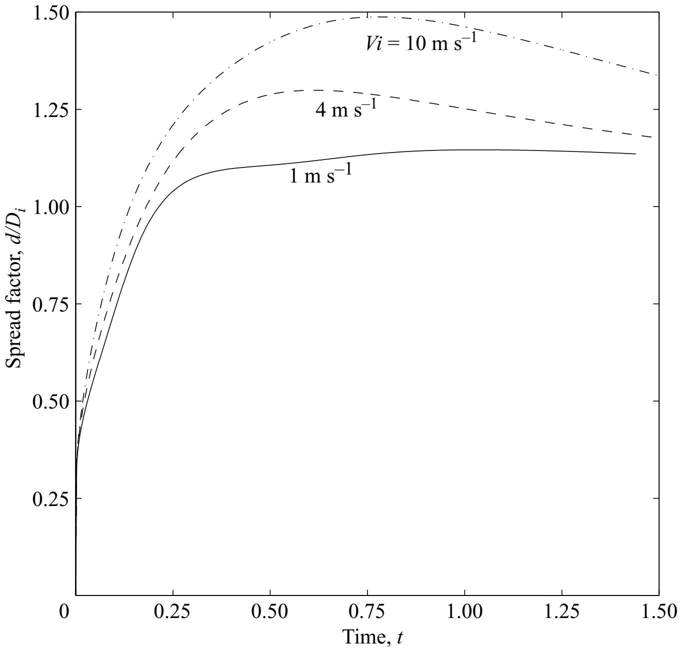

FIGURE 9. Effect of impact velocity on impact of 30 μm Pedot droplet. Other parameters are same as in figure 4.

6.5. *Effect of Weber number*

Figure 10 displays the influence of the Weber number on the impact process at a fixed *Re* of 13. Since *Re* is kept constant, *We* can only be varied by changing the surface tension and hence this can also be regarded as the effect of surface tension. The maximum value of the spread factor shows a slight increase from about 1.46 to 1.5 as *We* decreases from 150 to 1.5. This behaviour is in contradiction with the results reported on millimetre size droplets (Fukai *et al.* 1993; Pasandideh-Fard *et al.* 1996; Roisman *et al.* 2002) where an increase rather than a decrease of maximum value of the spread factor has been observed. This deviation may be due to a difference of about one or two orders-of-magnitude in the values of *Re* and *We* between the current micron-size case and millimetre-size studies reported in the literature. It seems that for $We \approx 1$ the capillary pressure, in addition to inertia, acts as a driving force for spreading, which may be possible as the initial droplet configuration is not the equilibrium configuration. Nevertheless, a decrease in time at which the maximum of spread factor is attained and subsequent, as expected, faster recoil of the droplet with a decrease in *We* is in accordance with the previous results on millimetre size droplets.

6.6. *Effect of Reynolds number*

The effect of the Reynolds number at a fixed $We = 1.5$ is studied by changing the droplet viscosity. The viscosity ratio is also changed accordingly so that the viscosity of the ambient fluid remains the same. Figure 11 shows that as the Reynolds number increases the extent of droplet spreading increases. Also, the time to reach the maximum spread factor shifts to later stages. This is due to the relative increase in the inertia that drives the flow compared to the viscous forces that oppose it. In fact,

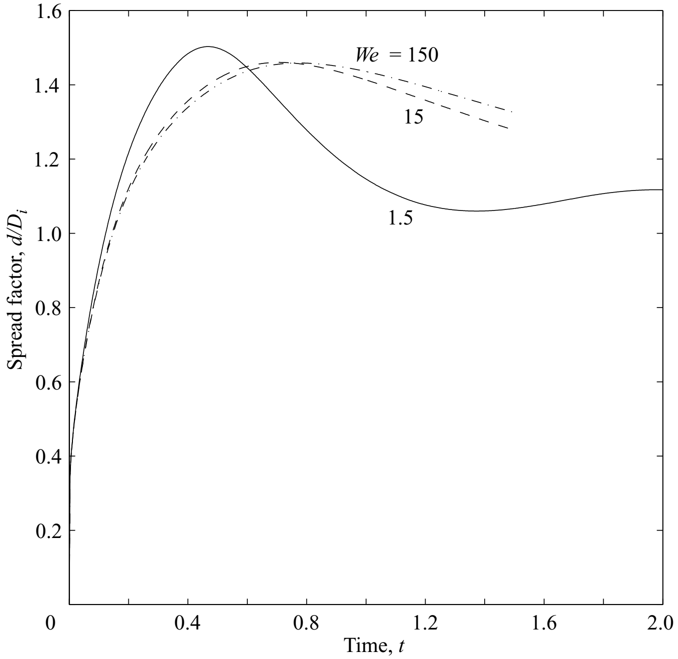

FIGURE 10. Effect of Weber number (surface tension) on droplet impact process at $Re = 13$ and $\theta = 90°$.

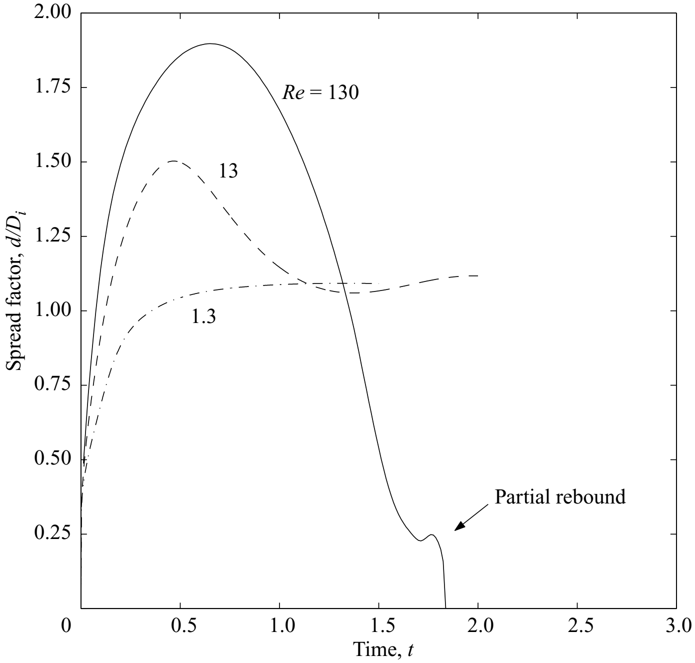

FIGURE 11. Effect of Reynolds number (droplet viscosity) on droplet impact process at $We = 1.5$ and $\theta = 90°$.

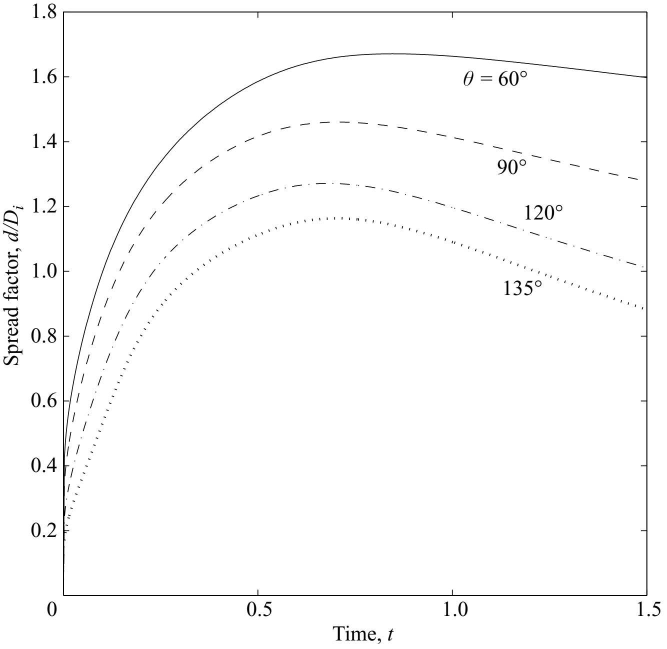

FIGURE 12. Effect of wettability on droplet impact process at $Re = 13$ and $We = 15$. Other parameters same as in figure 3.

for $Re = 1.3$ these two forces are almost equal and hence the droplet never spreads beyond its equilibrium value. As a consequence of the increased spreading the recoil behaviour is also affected, which leads to partial rebound of the droplet in the case of $Re = 130$.

6.7. *Effect of wettability*

Figure 12 shows the effect of the contact angle at a fixed $Re = 13$ and $We = 15$ where it is obvious that the contact angle affects the entire impact process. In particular, the maximum spread factor, the time to attain it and the time the droplet remains near the maximum spread factor increase with a decrease in the contact angle. This effect of contact angle, in accordance with the results of Fukai *et al.* (1995), on the impact behaviour holds even when We is decreased by a factor of ten to 1.5 and/or Re is increased to 130, as can be seen in figures 13 and 15. Also, with a decrease in We to 1.5, the surface tension becomes more dominant with its obvious effect on the recoil behaviour allowing us to understand better the influence of the contact angle on this stage of the process. For $Re = 13$, see figure 13, with an increase in the contact angle from $\theta = 60°$ to 90° the droplet oscillates more before stabilizing to an equilibrium value. These oscillations grow in size with a further increase in θ from 90° to 120°, until at $\theta \approx 135°$ the entire droplet lifts off from the solid surface, i.e. total rebound of the droplet occurs.

The effect of θ on the recoil behaviour at $Re = 130$ displays even richer phenomena as depicted in figures 14 and 15. Owing to high energy impact, the droplet in each case shows a central dry-out region at almost the same time and acquires a toroidal shape whose width increases with a decrease in the contact angle. After the spreading reaches a maximum the toroidal droplet recoils with a continuous decrease in the

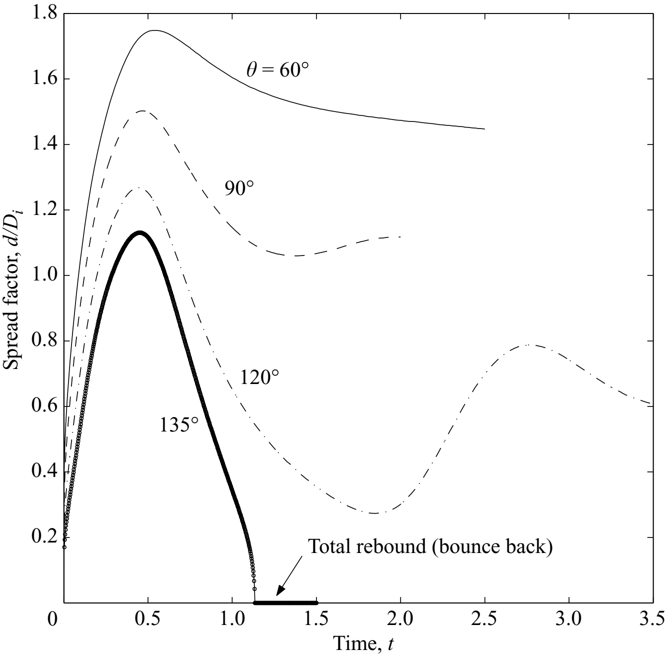

FIGURE 13. Effect of wettability on droplet impact process at $Re = 13$ and $We = 1.5$. Other parameters same as in figure 6.

size of the dry-out region and at some point in time, which again decreases with a increase in the contact angle, the inner side of the torus comes close enough to merge. The merging happens at the edge of the torus for contact angles smaller than 90° and near the apex, resulting in an entrapment of a small amount of ambient fluid, for contact angles greater than 90°. The size of the entrapped 'bubble', though larger for larger contact angles, is still smaller than the stable size dictated by the c^4 description of the free energy and hence it dissolves into the recoiling droplet. The recoiling halts and spreading restarts for $\theta = 45°$ at $t \approx 659\,\mu\text{s}$. The recoiling for $\theta = 60°$ and $90°$ results in a partial rebound of the droplet leaving progressively smaller amounts of the droplet on the solid surface that subsequently dissolves into the ambient fluid, while for $\theta = 120°$ the droplet breaks up into two unequal parts after total rebound of the droplet occurs. Owing to the solubility of physical nature inherent in the c^4 description of the free energy, as noted earlier, the smaller part of the droplet later dissolves, albeit at a physically unrealistic higher rate, into the ambient fluid. Note that a more immiscible system can be formulated either by decreasing the value of Cahn number or by modifying the description of the homogeneous part of the free energy with a higher (greater than c^4) approximation or using a Flory–Huggins type of free energy (Keestra *et al.* 2003) that may alleviate the observed dissolution. Here we prefer to use the classical and widely used c^4 approximation for the homogeneous part of the free energy since this a first attempt to model droplet impact using DIM.

6.8. *Influence of Péclet number*

The material-dependent mobility, analogous to the slip length in the slip models, is an important model parameter. It not only governs the contact line speed, via a

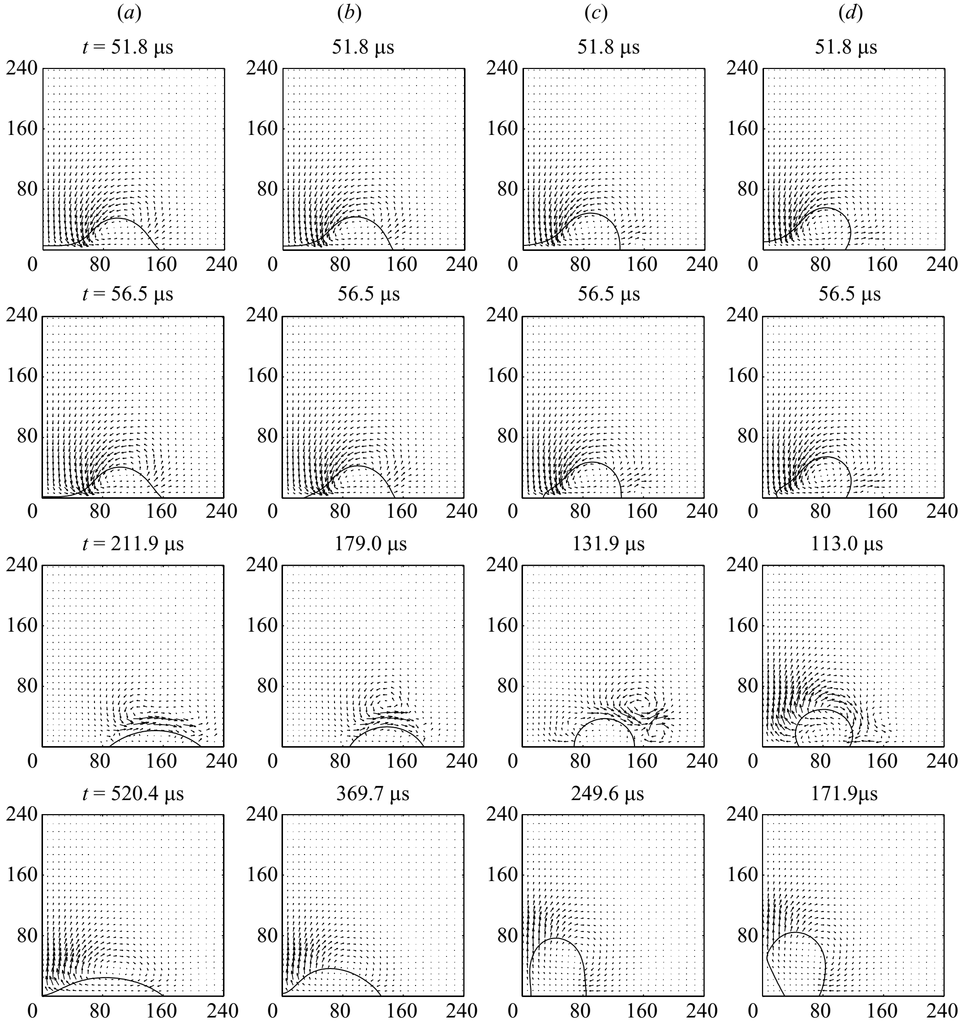

FIGURE 14. For caption see facing page.

diffusional flux in the cases where a no-slip velocity boundary is imposed, but also imparts the interface with certain resistance to convective straining (Jacqmin 1999). After non-dimensionalization of the governing equations this mobility is contained in the Péclet number. The Péclet number is therefore important, which is reflected in figure 16 where a comparison of the spread factor obtained using $Pe = 1$, 2.5, 5 and 10 is made. It is clear that the spreading behaviour is significantly affected by Pe. Increasing Pe or equivalently decreasing the mobility slows the process of spreading, i.e. the spreading rate is decreased, while the extent to which a drop spreads, except for $Pe = 10$, as characterized by the spread factor, remains roughly the same. For $Pe = 10$, contact-line pinning occurs which results in rupture of the central part of the droplet; creating a torus with dry-out.

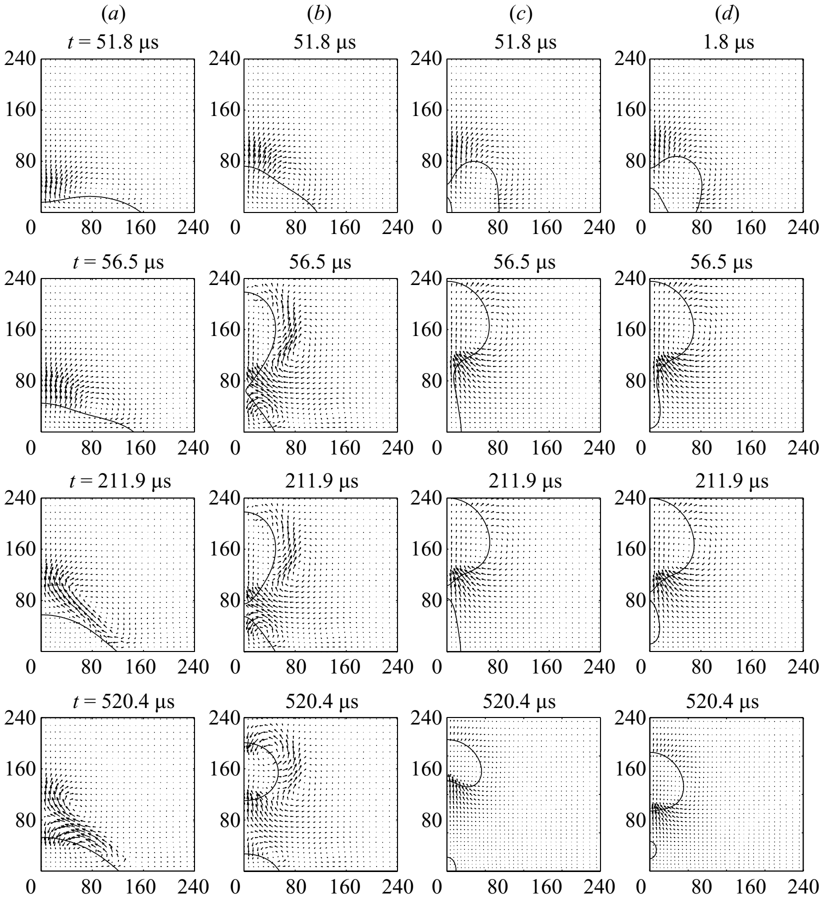

FIGURE 14. Influence of wettability on impact of a droplet of diameter of 157 μm impacting with a velocity of 0.83 m s^{-1} on a flat solid surface. (*a*) $\theta = 45°$, (*b*) $\theta = 60°$, (*c*) $\theta = 90°$ and (*d*) $\theta = 120°$. Other simulation parameters same as in figure 7.

Experimentally† no breakup was observed for the condition used in the simulation. So, $Pe = O(1)$ seems to be necessary for the resolution of the contact line singularity a when no-slip boundary is used, a condition met in Jacqmin (2000) where low-velocity flow was considered. A rough estimate of Pe gives a value of 7 (based on mobility in the gas phase) and a value of 70 000 (based on mobility in the liquid phase). For this estimation, the droplet diameter, the impact velocity, interface thickness, interfacial tension and the mobilities in the gas and liquid phases are assumed to be 50×10^{-6} m, 1 m s^{-1}, 10^{-9} m, 70×10^{-3} N m^{-1}, 10^{-13} m^5 s^{-1} J^{-1} and 10^{-17} m^5 s^{-1} J^{-1}, respectively. The values of mobility in the gas phase and liquid phase are typical values for gas diffusing in a gas and liquid diffusing in liquid in the absence of solid.

---

† Private communication with P. C. Duineveld who had performed some experiments under similar conditions in the context of another study. The main difference between our simulations and those experiments is that in the experiments the droplet material exhibited a zero receding contact angle with the solid surface.

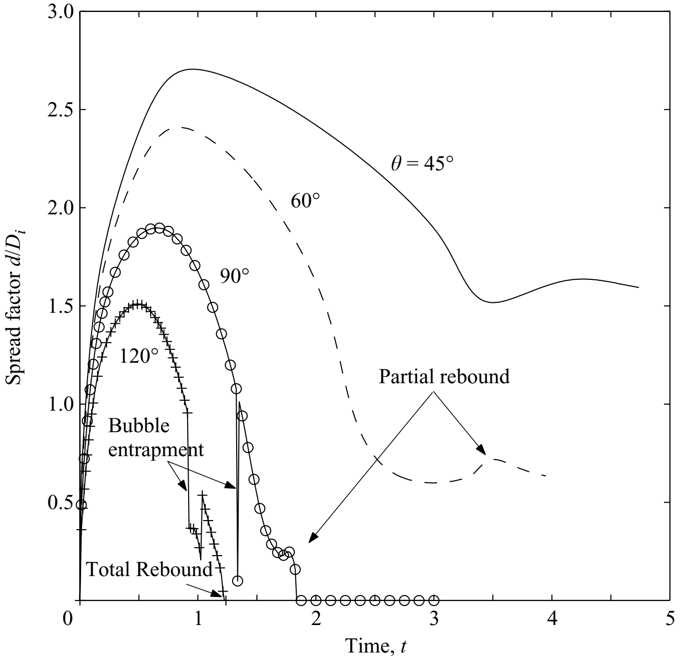

FIGURE 15. Effect of wettability on droplet impact process at $Re = 130$ and $We = 1.5$. Other parameters are the same as in figure 14.

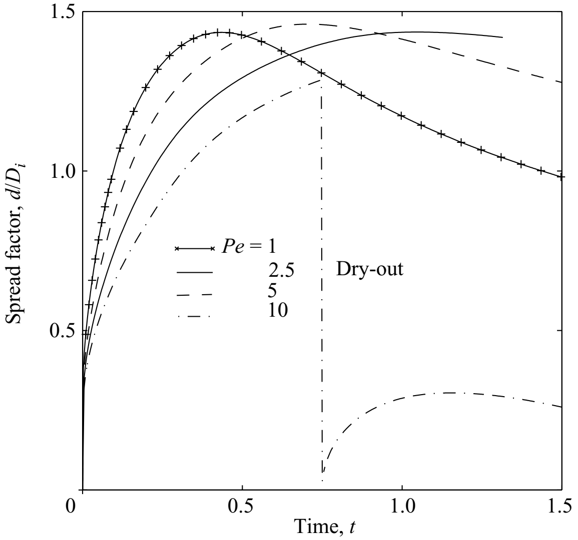

FIGURE 16. Effect of Péclet number on droplet impact process. Other parameters used are $C_h = 0.04$, $Re = 13$, $We = 15$, $\theta = 90°$ and $\lambda = 1000$.

6.9. *Effect of viscosity ratio*

The DIM, considered here, is a two-phase model with the droplet dynamics coupled to that of the ambient fluid which may affect the droplet spreading process. This is considered in this section by performing simulations for four different viscosity

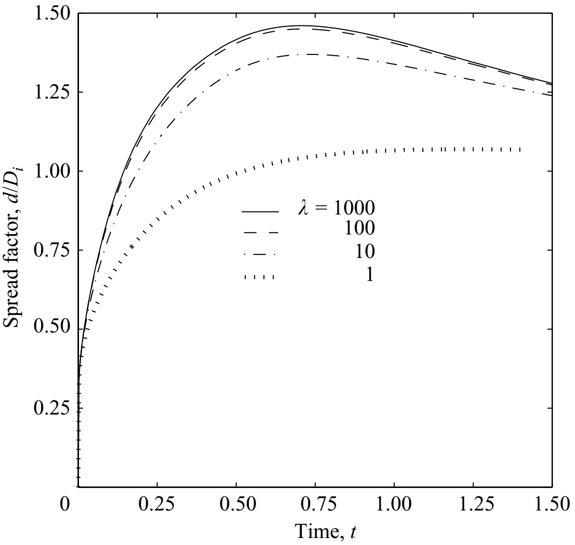

FIGURE 17. Effect of viscosity ratio on droplet impact process. Other parameters same as in figure 16.

ratios: 1, 10, 100 and 1000. Note that an increase in viscosity ratio means a decrease in ambient fluid viscosity. Figure 17 shows that a decrease in the viscosity of the ambient fluid leads to faster spreading.

7. Conclusion

A diffuse-interface model was applied to model the impact of micron-size droplets on a solid surface under conditions similar to those in inkjet printing. The model applied could capture droplet spreading, recoiling and rebounding (total and partial) off the solid surface. The viscosity of the droplet or more appropriately the Reynolds number is important during the spreading stage of the impact and in particular determines whether the droplet will spread beyond its equilibrium extent, i.e. whether recoiling will occur or not. During the droplet recoiling, the surface tension or equivalently the Weber number plays a significant role. The wettability of the solid surface was found to affect the entire impact process and was seen to have a dominant role in determining the outcome of the process.

This work is sponsored by the Dutch Polymer Institute (Project No. 178).

Appendix A. Specifying the initial velocity field

The prescribed initial velocity field should satisfy the equation of continuity, which in axisymmetric coordinates is given by (3.6). In previous studies which considered flow only inside the droplet and neglected the ambient fluid dynamics, the radial component u of the initial velocity field is assumed to be zero. Considering this assumption to be valid in the present two-phase flow case, (3.6) reduces to

$$\frac{\partial(\rho v)}{\partial z} = 0, \tag{A 1}$$

which upon integration yields

$$\rho v = K, \tag{A 2}$$

where K is the constant of integration. Requiring that inside the droplet v equals the impact velocity V_i, we find $K = \rho_d V_i$ and (A 2), after rearrangement, becomes

$$v = \frac{\rho_d}{\rho} V_i. \tag{A 3}$$

It is easy to see from (A 3) that outside the droplet, the axial velocity v is greater than (or at least equal to) the impact velocity V_i and not zero as is usually prescribed in studies using the classical sharp-interface model.

Appendix B. Rough estimate of the magnitude of the body force

Assuming that the droplet is a rigid sphere, (3.5) reduces to

$$Re\,\rho\left(\frac{\partial v}{\partial t}\right) = \frac{Bo_i}{Ca}\rho, \tag{B 1}$$

which upon integration, with v_0 denoting the initial velocity, yields

$$Re\left(\frac{v - v_0}{t}\right) = \frac{Bo_i}{Ca}. \tag{B 2}$$

Rearranging and noting that t equals Δt as gravity is applied only for one time step, leads to

$$Bo_i = Re\,Ca\frac{1}{\Delta t}. \tag{B 3}$$

REFERENCES

Anderson, D. M., McFadden, G. B. & Wheeler, A. A. 1998 Diffuse-interface methods in fluid mechanics. *Annu. Rev. Fluid Mech.* **30**, 139–165.

Anderson, P. D., Keestra, B. J. & Hulsen, M. A. 2006 On the streamfunction-vorticity formulation in sliding bi-period frames: Application to bulk behavior for polymer blends. *J. Comput. Phys.* **212**, 268–287.

Asai, A., Shioya, M., Hirasawa, S. & Okazaki, T. 1993 Impact of an ink drop on paper. *J. Imag. Sci. Tech.* **37**, 205–207.

Attinger, D. & Poulikakos, D. 2001 Melting and resolidification of a substrate caused by molten microdroplet impact. *Trans. ASME: J. Heat Transfer* **123**, 1110–1122.

Attinger, D., Zhao, Z. & Poulikakos, D. 2000 An experimental study of molten microdroplet surface deposition and solidification: Transient behavior and wetting angle dynamics. *Trans. ASME: J. Heat Transfer* **122**, 544–556.

Aziz, S. D. & Chandra, S. 2000 Impact, recoil and splashing of molten metal droplets. *Intl J. Heat Mass Transfer* **43**, 2841–2857.

Barosan, I., Anderson, P. D. & Meijer, H. E. H. 2006 Application of mortar elements to diffuse-interface methods. *Computers Fluids* **35** (10), 1384–1399.

Bergeron, V., Bonn, D., Martin, J. Y. & Vovelle, L. 2000 Controlling droplet deposition with polymer additives. *Nature* **405**, 772–775.

Beveridge, G. S. G. & Schechter, R. S. 1970 *Optimization: Theory and Practice*. McGraw-Hill.

Bhola, R. & Chandra, S. 1999 Parameters controlling solidification of molten wax droplets falling on a solid surface. *J. Mater. Sci* **34**, 4883–4894.

Blake, T. D. 1993 *Dynamic Contact Angles and Wetting Kinetics*. Surfactant Science Series, vol. 49. Marcel Dekker.

Boettinger, W. J., Warren, J. A., Beckermann, C. & Karma, A. 2002 Phase-field simulation of solidification. *Annu. Rev. Mater. Res.* **32**, 163–194.

Briant, A. J., Wagner, A. J. & Yeomans, J. M. 2004 Lattice Boltzmann simulations of contact line motion. I. Liquid-gas systems. *Phys. Rev.* E **69**, 031602.

Briant, A. J. & Yeomans, J. M. 2004 Lattice Boltzmann simulations of contact line motion. II. Binary fluids. *Phys. Rev.* E **69**, 031603.

Bussmann, M., Mostaghimi, J. & Chandra, S. 1999 On a three-dimensional volume tracking model of droplet impact. *Phys. Fluids* **11**, 1406–1417.

Cahn, J. W. 1964 Phase separation by spinodal decomposition in isotropic systems. *J. Chem. Phys.* **42** (1), 93–99.

Cahn, J. W. 1977 Critical point wetting. *J. Chem. Phys.* **66** (8), 3667–3672.

Cahn, J. W. & Hilliard, J. E. 1958 Free energy of a nonuniform system. I. Interfacial energy. *J. Chem. Phys.* **28** (2), 258–267.

Chandra, S. & Avedisian, C. T. 1991 On the collision of a droplet with a solid surface. *Proc. R. Soc. Lond.* A **432**, 13–41.

Chella, R. & Viñals, J. 1996 Mixing of a two-phase fluid by cavity flow. *Phys. Rev.* E **53** (4), 3832–3840.

Chen, H.-Y., Jasnow, D. & Viñals, J. 2000 Interface and contact line motion in a two phase fluid under shear flow. *Phys. Rev. Lett.* **85** (8), 1686–1689.

Crooks, R. C. & Boger, D. V. 2001 Influence of fluid elasticity on drop impacting on dry surfaces. *J. Rheol.* **44**, 973–996.

Crooks, R. C., Cooper-White, J. J. & Boger, D. V. 2001 The role of dynamic surface tension and elasticity in the dynamics of drop impact. *Chem. Engng Sci.* **56**, 5575–5592.

Crooks, R. C., Cooper-White, J. J. & Boger, D. V. 2002 A drop impact study of worm-like viscoelastic surfactant solutions. *Colloids Surf.* A **210**, 105–123.

van Dam, D. B. & Clerc, C. L. 2004 Experimental study of the impact of an ink-jet printed droplet on a solid substrate. *Phys. Fluids* **16**, 3403–3414.

Davis, H. T. & Scriven, L. E. 1982 Stress and structure in fluid interfaces. *Adv. Chem. Phys.* **49**, 357–454.

Duineveld, P. 2003 The stability of ink-jet printed lines of liquid with zero receding contact angle on a homogeneous substrate. *J. Fluid Mech.* **477**, 175–200.

Dussan V., E. B. & Davis, S. H. 1974 On the motion of a fluid-fluid interface along a surface. *J. Fluid Mech.* **65**, 71–95.

Fedorchenko, A. I., Wang, A.-B. & Wang, Y.-H. 2005 Effect of capillary and viscous forces on spreading of a liquid drop impinging on a solid surface. *Phys. Fluids* **17**, 0931041–0931048.

Fournier, A., Bunge, H. P., Hollerbach, R. & Villote, J. P. 2004 Application of the spectral-element method to the axisymmetric Navier-Stokes equation. *Geophys. J. Intl* **156**, 682–700.

Francois, M. & Shyy, W. 2003 Computations of drop dynamics with the immersed boundary method, Part 2: Drop impact and heat transfer. *Numer. Heat Transfer* B **44**, 119–143.

Fukai, J., Shiiba, Y., Yamamoto, T., Miyatake, O., Poulikakos, D., Megaridis, C. M. & Zhao, Z. 1995 Wetting effects on the spreading of a liquid droplet colliding with a flat surface: Experiment and modeling. *Phys. Fluids* **7**, 236–247.

Fukai, J., Zhao, Z., Poulikakos, D., Megaridis, C. M. & Miyatake, O. 1993 Modeling of the deformation of a liquid droplet impinging upon a flat surface. *Phys. Fluids* **5**, 2588–2599.

de Gans, B.-J., Duineveld, P. & Schubert, U. S. 2004 Inkjet printing of polymers: State of the art and future developments. *Adv. Mater.* **16**, 203–213.

de Gennes, P. G. 1985 Wetting: statics and dynamics. *Rev. Mod. Phys.* **57**, 827–862.

Gerritsma, M. I. & Phillips, T. N. 2000 Spectral element methods for axisymmetric Stokes problem. *J. Comput. Phys.* **164**, 81–103.

Gunjal, P. R., Ranade, V. V. & Chaudhari, R. V. 2005 Dynamics of drop impact on solid surface: Experiments and VOF simulations. *AIChE J.* **51**, 59–78.

Gunton, J. D., Miguel, M. S. & Sahni, P. S. 1983 *The Dynamics of First-order Phase Transitions.* Phase Transitions and Critical Phenomena, vol. 8. Academic.

Hocking, L. M. 1977 A moving fluid interface. Part 2. The removal of force singularity by a slip flow. *J. Fluid Mech.* **79**, 209–229.

Huh, C. & Scriven, L. E. 1971 Hydrodynamic model of steady movement of a solid/liquid/fluid contact line. *J. Colloid Interface Sci.* **35**, 85–100.

Jacqmin, D. 1999 Calculation of two-phase Navier-Stokes flows using phase-field modeling. *J. Comput. Phys.* **155**, 96–127.

Jacqmin, D. 2000 Contact-line dynamics of a diffuse fluid interface. *J. Fluid Mech.* **402**, 57–88.

Jasnow, D. & Viñals, J. 1996 Coarse-grained description of thermo-capillary flow. *Phys. Fluids* **8** (3), 660–669.

Joseph, D. D. & Renardy, Y. Y. 1993 *Fundamentals of Two-fluid Dynamics*. Springer.

Kawase, T., Shimoda, T., Newsome, C., Sirringhaus, H. & Friend, R. H. 2003 Inkjet printing of polymer thin film transistor. *Thin Solid Films* **438–439**, 279–287.

Keestra, B. J., van Puyvelde, P. C. J., Anderson, P. D. & Meijer, H. E. H. 2003 Diffuse interface modeling of the morphology and rheology of immiscible polymer blends. *Phys. Fluids* **15**, 2567–2575.

Khatavkar, V. V., Anderson, P. D. & Meijer, H. E. H. 2006 On scaling of diffuse-interface models. *Chem. Engng Sci.* **61** (8), 2364–2378.

Khatavkar, V. V., Anderson, P. D. & Meijer, H. E. H. 2007 Capillary spreading of droplet in a partially wetting regime using a diffuse-interface model. *J. Fluid Mech.* **572**, 367–387.

Kim, H.-Y., Park, S.-Y. & Min, K. 2003 Imaging high-speed impact of mircodrop on solid surface. *Rev. Sci. Instrum.* **74**, 4930–4937.

Lee, H.-G., Lowengrub, J. S. & Goodman, J. 2002*a* Modeling pinchoff and reconnection in a Hele-Shaw cell. I. The models and their calibration. *Phys. Fluids* **14** (2), 492–513.

Lee, H.-G., Lowengrub, J. S. & Goodman, J. 2002*b* Modeling pinchoff and reconnection in a Hele-Shaw cell. II. Analysis and simulation in the non-linear regime. *Phys. Fluids* **14** (2), 514–545.

Lowengrub, J. & Truskinovsky, L. 1998 Quasi-incompressible Cahn Hilliard fluids. *Proc. R. Soc. Lond.* A **454**, 2617–2654.

Mao, T., Kuhn, D. C. S. & Tran, H. 1997 Spread and rebound of liquid droplets upon impact on flat surfaces. *AIChE J.* **43**, 2169–2179.

Naumann, E. & He, D. 2001 Nonlinear diffusion and phase separation. *Chem. Engng Sci.* **56**, 1999–2018.

Okamoto, T., Suzuki, T. & Yamamoto, N. 2000 Microarray fabrication with covalent attachment of DNA using bubble jet technology. *Nat. Biotechnol.* **18**, 438–441.

Park, H., Carr, W. W., Zhu, J. & Morris, J. F. 2003 Single drop impaction on a solid surface. *AIChE J.* **49**, 2461–2471.

Pasandideh-Fard, M., Qiao, Y. M., Chandra, S. & Mostaghimi, J. 1996 Capillary effects during droplet impact on a solid surface. *Phys. Fluids* **8**, 650–659.

Pasandideh-Fard, M., Qiao, Y. M., Chandra, S. & Mostaghimi, J. 2002 On a three-dimensional model of droplet impact and solidification. *Intl J. Heat Mass Transfer* **45**, 2229–2242.

Patera, A. T. 1984 A spectral element method for fluid dynamics. *J. Comput. Phys.* **54**, 468–488.

Range, K. & Feuillebois, F. 1998 Influence of surface roughness on liquid drop impact. *J. Colloid Interface Sci.* **203**, 16–30.

Rein, M. 1993 Phenomena of liquid drop impact on solid and liquid surfaces. *Fluid Dyn. Res.* **12**, 61–93.

Renardy, M., Renardy, Y. & Li, J. 2001 Numerical simulation of moving contact line problems using a volume-of-fluid method. *J. Comput. Phys.* **171**, 243–263.

Renardy, Y., Popinet, S., Duchemin, L., Renardy, M., Zaleski, S., Josserand, C., Drumright-Clarke, M. A., Richard, D., Clanet, C. & Quere, D. 2003 Pyramidal and toroidal water drops after impact on a solid surface. *J. Fluid Mech.* **484**, 69–83.

Roisman, I. V., Rioboo, R. & Tropea, C. 2002 Normal impact of a liquid drop on a dry surface: model for spreading and receding. *Proc. R. Soc. Lond.* A **458**, 1411–1430.

Rowlinson, J. S. & Widom, B. 1989 *Molecular Theory of Capillarity*. Clarendon.

Schiaffino, S. & Sonin, A. 1997 Molten droplet deposition and solification at low Weber number. *Phys. Fluids* **9**, 3172–3187.

Segal, A. 1995 *SEPRAN manual*. Leidschendam, The Netherlands.

Sekerka, R. 2004 Morphology: from sharp interface to phase field models. *J. Crystal Growth* **264**, 530–540.

Seppecher, P. 1996 Moving contact lines in the Cahn–Hilliard theory. *Intl J. Engng Sci.* **34** (9), 977–992.

Šikalo, Š., Wilhelm, H.-D., Roisman, I. V., Jakirlič, S. & Tropea, C. 2005 Dynamic contact angle of spreading droplets: Experiments and simulations. *Phys. Fluids* **17**, 0621031–06210313.

SIRRINGHAUS, H., KAWASE, T., FRIEND, R. H., SHIMODA, T., INBASEKARAN, M., WU, W. & WOO, E. P. 2000 High-resolution inkjet printing of all-polymer transistor circuits. *Science* **290**, 2123–2126.

TIMMERMANS, L. J. P., VAN DE VOSSE, F. N. & MINEV, P. D. 1994 Taylor-Galerkin-based spectral element methods for convection-diffusion problems. *Intl J. Numer. Meth. Fluids* **18**, 853–870.

VERSCHUEREN, M. 1999 A diffuse-interface model for structure development in flow. PhD thesis, Eindhoven University of Technology, The Netherlands (downloadable from http://www.mate.tue.nl/mate/pdfs/56.pdf).

VERSCHUEREN, M., VAN DE VOSSE, F. N. & MEIJER, H. E. H. 2000 Diffuse-interface modelling of thermocapillary flow instabilities in a Hele-Shaw cell. *J. Fluid Mech.* **434**, 153–166.

VAN DER WAALS, J. D. 1893 The thermodynamic theory of capillarity under the hypothesis of a continuous variation of density. *Verhandel. Konink. Akad. Weten. Amsterdam* **1** (English translation by J. S. Rowlinson in *J. Statist. Phys.* **20** (1979), 197–244).

WORTHINGTON, A. M. 1876 On the forms assumed by drops of liquids falling vertically on a horizontal plate. *Proc. R. Soc. Lond.* A **25**, 261–271.

YARIN, A. L., YAZICIOGLU, A. G., MEGARIDIS, C. M., ROSSI, M. P. & GOGOTSI, Y. 2005 Theoretical and experimental investigation of aqueous liquids contained in carbon nanotubes. *J. Appl. Phys.* **97**, 1243091.

YUE, P., FENG, J. J., LIU, C. & SHEN, J. 2004 A diffuse-interface method for simulating two-phase flows of complex fluids. *J. Fluid Mech.* **515**, 293–317.

ZHANG, X. & BASARAN, O. A. 1997 Dynamic Surface Tension Effects in Impact of a Drop with a Solid Surface. *J. Colloid Interface Sci.* **187**, 166–178.

ZHAO, Z., POULIKAKOS, D. & FUKAI, J. 1996*a* Heat transfer and fluid dynamics during the collision of a liquid droplet on a substrate-I. Modeling. *Intl J. Heat Mass Transfer* **39**, 2771–2789.

ZHAO, Z., POULIKAKOS, D. & FUKAI, J. 1996*b* Heat transfer and fluid dynamics during the collision of a liquid droplet on a substrate-II. Experiments. *Intl J. Heat Mass Transfer* **39**, 2791–2802.